

HOW PHYSICAL AND CHEMICAL PROPERTIES CHANGE ICE NUCLEATION
EFFICIENCY OF SOOT AND POLYAROMATIC HYDROCARBON PARTICLES

A Thesis

by

KATIE ANN SUTER

Submitted to the Office of Graduate Studies of
Texas A&M University
in partial fulfillment of the requirements for the degree of

MASTER OF SCIENCE

August 2011

Major Subject: Atmospheric Sciences

HOW PHYSICAL AND CHEMICAL PROPERTIES CHANGE ICE NUCLEATION
EFFICIENCY OF SOOT AND POLYAROMATIC HYDROCARBON PARTICLES

A Thesis

by

KATIE ANN SUTER

Submitted to the Office of Graduate Studies of
Texas A&M University
in partial fulfillment of the requirements for the degree of

MASTER OF SCIENCE

Approved by:

Chair of Committee,
Committee members,

Head of Department,

Sarah Brooks
Renyi Zhang
Richard Lee Panetta
William Marlow
Kenneth Bowman

August 2011

Major Subject: Atmospheric Sciences

ABSTRACT

How Physical and Chemical Properties Change Ice Nucleation Efficiency of Soot and Polyaromatic Hydrocarbon Particles. (August 2011)

Katie Ann Suter, B.S., Texas A&M University

Chair of Advisory Committee: Dr. Sarah Brooks

Heterogeneous freezing processes in which atmospheric aerosols act as ice nuclei (IN) cause nucleation of ice crystals in the atmosphere. Heterogeneous nucleation can occur through several freezing mechanisms, including contact and immersion freezing. The mechanism by which this freezing occurs depends on the ambient conditions and composition of the IN. Aerosol properties change through chemical aging and reactions with atmospheric oxidants such as ozone.

We conducted a series of laboratory experiments using an optical microscope apparatus equipped with a cooling stage to determine how chemical oxidation changes the ability of atmospheric aerosols to act as IN. Freezing temperatures are reported for aerosols composed of fresh and oxidized soot and polyaromatic hydrocarbons (PAHs) including anthracene, phenanthrene, and pyrene.

Our results show that oxidized soot particles initiate ice freezing events at significantly warmer temperatures than fresh soot, 3 °C on average. All oxidized PAHs studied had significantly warmer freezing temperatures than fresh samples. The chemical changes presumably causing the improved ice nucleation efficiency were observed using

Fourier Transform Infrared Spectroscopy with Horizontal Attenuated Total Reflectance.

The addition of C=O bonds at the surface of the soot and PAHs led to changes in freezing temperatures. Finally, we used classical nucleation theory to derive heterogeneous nucleation rates for the IN compositions in this research.

The overall efficiency of the IN can be compared in order of least efficient to most efficient: fresh phenanthrene, fresh anthracene, fresh soot, oxidized phenanthrene, fresh pyrene, oxidized anthracene, oxidized soot, and oxidized pyrene. Overall oxidation of aerosols increases their ability to act as IN. Our results suggest that oxidation processes facilitate freezing at warmer temperatures at a broader range of conditions on the atmosphere.

ACKNOWLEDGEMENTS

I would like to thank my committee chair, Dr. Sarah Brooks, and my committee members, Dr. Lee Panetta, Dr. Renyi Zhang and Dr. William Marlow, for their guidance and support throughout the course of this research.

I would like to thank my research group members for all their helpful ideas and assistance with this study. I thank the Department of Atmospheric Science faculty and staff for making my time at Texas A&M University a great experience. I also want to extend my gratitude to the National Science Foundation (NSF) for providing the funding for this study.

Thanks also go to my friends and family for their constant love and support. A special acknowledgement goes to my fiancé, David, who never ceases to tell me how proud he is of my accomplishments. Finally, thanks to my mother and father for their encouragement and love that has kept me going for the past 24 years. I don't think they really thought I would end up pursuing my dream of being a meteorologist since age 5. I also want to thank God for blessing me with the knowledge to complete this degree and the desire to start it in the first place.

TABLE OF CONTENTS

	Page
ABSTRACT	iii
ACKNOWLEDGEMENTS	v
TABLE OF CONTENTS	vi
LIST OF FIGURES	viii
LIST OF TABLES	xi
1. INTRODUCTION.....	1
2. EXPERIMENTAL METHODS	9
2.1 Sample Preparation	9
2.2 Fourier Transform Infrared Spectroscopy-Horizontal Attenuated Total Reflectance Experiments	11
2.3 Ice Nucleation Efficiency Experiments	14
2.4 Brunauer-Emmett-Teller (BET) Method	23
3. RESULTS AND DISCUSSION	29
3.1 FTIR Results	29
3.1.1 FTIR Results for PAHs	29
3.1.2 FTIR Results for Soot.....	35
3.2 Calibration of the Cold Stage	37
3.3 Results of Fresh and Oxidized Soot as IN.....	39
3.3.1 Soot Statistics.....	43
3.3.2 Discussion of Soot Results	46
3.4 Results of Fresh and Oxidized PAHs as IN	49
3.4.1 PAH Statistics	52
3.4.2 Discussion of PAHs as IN	54
3.5 BET Results.....	57
3.6 Application of Classical Nucleation Theory	59
3.6.1 Probability of Freezing.....	61
3.6.2 Heterogeneous Nucleation Rates for Soot and PAHs	68

	Page
3.6.3 Evaluation of Further Constraints on Nucleation Theory	75
4. ATMOSPHERIC IMPLICATIONS AND CONCLUSIONS.....	82
REFERENCES.....	86
VITA	91

LIST OF FIGURES

FIGURE	Page
1 The polar functional groups formed after ozone oxidizes the external rings of the soot	3
2 The four ways ice can be formed through heterogeneous processes are shown	4
3 From top: Olive oil (black), 137 μm oxidized soot mixed with olive oil (blue), and the difference spectrum of 137 μm oxidized soot plus olive oil-olive oil (red) allows just the spectrum of 137 μm oxidized soot to remain.	13
4 Experimental design of ice microscope	15
5 Unfrozen (a) and frozen (b) droplet with fresh soot acting as IN for contact freezing.....	19
6 Unfrozen (a) and frozen (b) droplet with oxidized soot acting as IN for immersion freezing	19
7 One experiment (137 μm oxidized soot) containing 33 cycles where there is little variability.	20
8 Variability within one experiment (fresh 50 μm soot) is seen due to possible particle repositioning.....	21
9 Adsorption isotherm of Kr on fresh 45-53 μm lampblack soot	27
10 Linearized form of the BET isotherm for the adsorption of Kr on 0.019 g of 45-53 μm fresh lampblack soot.....	27
11a Fresh Anthracene spectrum (cm^{-1})	30
11b Fresh Phenanthrene spectrum (cm^{-1}).....	30
11c Fresh Pyrene spectrum (cm^{-1}).....	30

FIGURE	Page
12 Fresh (black), oxidized (blue), and the difference spectrum of oxidized-fresh (red) of anthracene show new bonds formed after ozone exposure	31
13 Fresh (black), oxidized (blue), and the difference spectrum of oxidized-fresh (red) of phenanthrene show new bonds formed after ozone exposure	33
14 Fresh (black), oxidized (blue), and the difference spectrum of oxidized-fresh (red) of pyrene show new bonds formed after ozone exposure	34
15 Oxidized 137 μm soot (black) and fresh 275 μm soot (blue) shows growth of C=O bond between 1600 and 1800 cm^{-1} after ozone exposure.....	36
16 Using yellow sand as the IN, the humidified flow was turned off allowing the experiment to run until evaporation.....	37
17 Freezing event temperatures for 275 μm diameter fresh (blue) and oxidized (red) soot particles	40
18 Freezing event temperatures for 137 μm diameter fresh (pink) and oxidized (light blue) soot particles	41
19 Freezing event temperatures for 50 μm diameter fresh (orange) and oxidized (green) soot particles	41
20 Freezing event temperatures for fresh (purple) and oxidized (green) anthracene particles	49
21 Freezing event temperatures for fresh (navy) and oxidized (orange) phenanthrene particles.....	50
22 Freezing event temperatures for fresh (red) and oxidized (gray) pyrene particles	50
23a Empirical probability curves for fresh (black) and oxidized (green) soot and theoretical probability curves for fresh and oxidized soot (blue)	63

FIGURE	Page
23b Empirical probability curves for fresh (purple triangles) and oxidized (blue x) anthracene and theoretical probability curves for fresh and oxidized anthracene (green line)	63
23c Empirical probability curves for fresh (red diamonds) and oxidized (green circles) phenanthrene and theoretical probability curves for fresh and oxidized (navy line) phenanthrene	64
23d Empirical probability curves for fresh (aqua diamonds) and oxidized (pink circles) pyrene and theoretical probability curves for fresh and oxidized (red line) pyrene.....	64
24 The empirical probability curves for each size of fresh and oxidized soot are shown: fresh 275 μm (black), oxidized 275 μm (blue), fresh 137 μm (red), oxidized 137 μm (green), fresh 50 μm (purple), and oxidized 50 μm (orange)	67
25a Calculated normalized heterogeneous nucleation rates ($\text{cm}^{-2}\text{sec}^{-1}$) using best fit of f are shown.	72
25b The percentage of droplets containing a specific IN that have nucleated in one minute at a specific temperature is reported.....	73
26 The surface of each particle is divided into a number n_{site} of surface sites, which are characterized by contact angles that have a certain energy barrier	79
27 Probability curves similar to those in this study are shown	80

LIST OF TABLES

TABLE	Page
1 List of PAHs to be used in this research	7
2 Mean freezing temperatures and pooled standard deviations for fresh and oxidized soot of each size	43
3 Statistical data are shown for fresh and oxidized soot of the same size	45
4 Statistical data are shown for fresh soot comparing the different sizes	45
5 Statistical data are shown for oxidized soot comparing the different sizes	45
6 Mean freezing temperatures and pooled standard deviations for fresh and oxidized anthracene, phenanthrene, and pyrene	51
7 The freezing mechanisms for each IN of this study	52
8a Statistical data are shown for fresh and oxidized PAHs	53
8b Statistical data are shown to compare each fresh PAH and each oxidized PAH	53
9 BET surface area based on mass for fresh soot.....	58
10 BET surface area based on mass for oxidized soot.....	58
11 Calculated wetting parameter, f , for all IN sizes and compositions in this study are reported	65
12 Heterogeneous nucleation rates, J (single particle) and J (normalized), for fresh and oxidized PAHs	73
13 Different sizes of soot are compared using nucleation rates, J (single particle) and J (normalized)	74

TABLE	Page
14 The best fit value of f , J (with surface area) and J (normalized) for oxidized and fresh soot using BET surface area measurements	77

1. INTRODUCTION

An aerosol is defined as a liquid or solid particle suspended in the atmosphere [Seinfeld and Pandis, 2006]. Aerosols provide surfaces for heterogeneous reactions and act as cloud condensation nuclei (CCN) or ice nuclei (IN), which affect atmospheric chemistry and climate. Aerosols can influence cloud microphysics and alter the radiation budget, leading to both indirect and direct effects on climate change [IPCC, 2007]. There is uncertainty in the amount of negative forcing that aerosols cause. Thus, more research is needed for accurate forcing estimates, especially in regard to the aging process. Furthermore, aerosols are important due to their ubiquity in the atmosphere.

Aerosols are emitted into the atmosphere from anthropogenic and natural sources. Natural sources include plant emissions, fires, dust, and sea salt [Seinfeld and Pandis, 2006]. Anthropogenic sources include incomplete combustion from industrial processes and biomass burning [Seinfeld and Pandis, 2006]. Major products of biomass burning and incomplete combustion are carbonaceous aerosols, including black carbon (soot), which are commonly found in urban and rural areas. The total amount of soot emitted by natural and anthropogenic sources has been estimated to be 24 Tg/y, and a total of 10 to 50% of all tropospheric particulates are carbonaceous in nature [Lary *et al.*, 1999; Penner *et al.*, 1993].

This thesis follows the style of *Journal of Geophysical Research*.

Soot particles are a complicated class of aerosols that interact with atmospheric processes and the radiative budget. By scattering and absorbing solar radiation, soot particles have a direct radiative forcing, and therefore a direct influence on climate change [IPCC, 2007]. Soot can indirectly affect climate through interactions with cloud processing and by acting as CCN or IN [IPCC, 2007]. These interactions can lead to an increase in cloud albedo and decreased precipitation [Rosenfeld, 2000]. For these reasons, soot is a principal focus of this study.

When freshly emitted, soot is hydrophobic in nature [Decesari *et al.*, 2002; Lary *et al.*, 1999; Weingartner *et al.*, 1997]. Fresh soot can act as CCN; however as IN, soot aerosols do not activate until temperatures are cold (< -20 °C) [Decesari *et al.*, 2002; Demott, 1990; Kotzick *et al.*, 1997]. For this reason, fresh soot particles are considered inefficient IN [Demott, 1990; Gorbunov *et al.*, 2001]. However, when soot is exposed to oxidants such as ozone (O₃), hydroxyl radical, UV light and oxygen, it becomes oxidized (or aged). The aging of soot may occur through several processes. Sulfur oxidation occurs on the surface of soot particles when in a humid environment [Finlayson-Pitts and Pitts, 2000]. There is a strong affinity of soot surfaces for organic compounds, which easily oxidize the soot surface [Lary *et al.*, 1999]. Different nitrogen compounds like HONO, NO₂, and HNO₃ have also been shown to oxidize of the soot surface. All these oxidation processes for soot are of importance to atmospheric chemistry. In addition, aging causes soot particles to become hydrophilic in nature and possibly become more efficient CCN and IN [Dymarska *et al.*, 2006; Weingartner *et al.*, 1997]. Fourier Transform Infrared Spectroscopy (FTIR) studies reveal that the chemical

transformation of soot leads to this change in hygroscopicity. FTIR shows that polar acidic oxygen-containing functional groups, known as carboxylic acids, are generated on the soot surface during oxidation with O_3 , the chosen oxidant for this study. The carboxylic acids facilitate water uptake in the condensation process and allow soot particles to activate at lower supersaturations [Chughtai *et al.*, 1991; Kotzick *et al.*, 1997]. The number of these oxygen containing groups depends on the oxidizing agent and the surface on which they occur [Lary *et al.*, 1999]. Figure 1 shows the structure of polar functional groups, like carboxylic acids, that form on the surface of soot after ozone exposure.

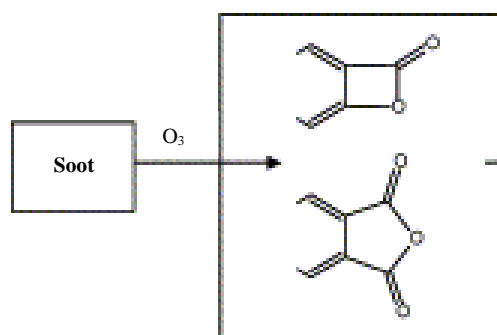


Figure 1. The polar functional groups formed after ozone oxidizes the external rings of the soot. Adapted from Decesari *et al.* [2002].

Changes in acidity and formation of oxygen-containing groups help explain the changes in hygroscopicity. Previous research shows soot particles are more likely to activate as CCN or IN after oxidation by O_3 [Kotzick and Niessner, 1999]. A goal of this study is to verify that exposing soot to O_3 causes a change in hygroscopicity, thereby

allowing freezing events at warmer temperatures. Previous studies have also explored both fresh and oxidized soot as IN using a variety of freezing mechanisms [Diehl and Mitra, 1998; Popovicheva et al., 2008a].

Homogeneous nucleation is the formation of ice without the presence of IN. Homogeneous freezing for droplets of an atmospherically relevant size occurs at or below $-40\text{ }^{\circ}\text{C}$, far below that of average tropospheric temperatures [Yau, 1989]. In the atmosphere, pure water rarely freezes into ice. Instead, ice forms through homogeneous freezing of a solution or ice forms with the help of IN by one of the heterogeneous freezing mechanisms: deposition, condensation, contact, or immersion [Vali, 1985]. Figure 2 illustrates the four main heterogeneous mechanisms.

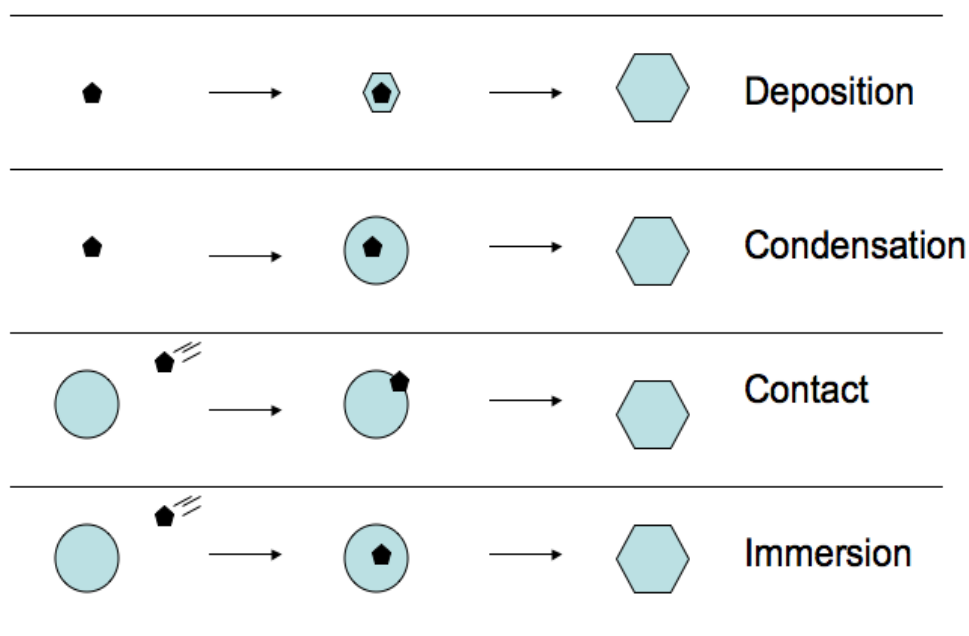


Figure 2. The four ways ice can be formed through heterogeneous processes are shown. The last two are the focus of this research. *Brooks Group*

Immersion freezing occurs when a supercooled droplet freezes due to an ice nucleus suspended in the middle of a water droplet [Vali, 1985]. This definition of immersion freezing appropriately expresses how immersion measurements for this research are obtained. Contact freezing occurs when a supercooled water droplet freezes due to an ice nucleus contacting the surface of the droplet [Vali, 1985]. Traditionally, contact freezing implied a collision occurred between an aerosol particle and a water droplet [Cooper, 1974; Fletcher, 1969; Fukuta, 1975]. Theoretically, dry IN provide a template at the surface of the droplet that can initiate freezing. Aerosols that act as IN are usually insoluble in water and have crystallographic structures similar to the ice lattice that provide active sites for nucleation. These active sites on IN are preferred sites of nucleation due to the particle-ice interfacial free energy being minimal [Fletcher, 1969; Niedermeier *et al.*, 2011; Vali, 2008]. Particles that are known to serve as IN include dust and combustion particles [Seinfeld and Pandis, 2006].

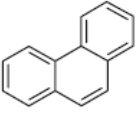
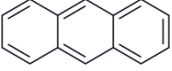
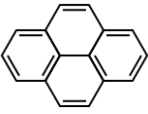
Recent studies provide insight on the driving force of contact freezing events. These studies suggest that it is the presence of IN at the surface of the droplet that reduces the surface free energy and facilitates freezing. An actual collision is not necessary to cause the freezing event. For example, Shaw *et al.* [2005] and Durant and Shaw [2005] observe freezing events as the droplet temperature drops at a constant rate while an aerosol particle sits at the water-air interface [Durant and Shaw, 2005; Shaw *et al.*, 2005]. They refer to this mode of freezing as “contact freezing inside-out” to distinguish it from collisional contact freezing. Their results show that contact freezing temperatures are identical whether the ice nucleus is placed outside or inside the droplet surface

[*Durant and Shaw, 2005; Shaw et al., 2005*]. Durant and Shaw's results ultimately indicate that IN do not need to be dry to be effective, but do need to contact the surface.

Differences that occur in freezing mechanisms due to the aging process also need more clarification. Ice nucleation is undoubtedly an important mechanism in the atmosphere. When conducting ice nucleation experiments, it is important to study a variety of techniques, particle compositions, and controls. There is uncertainty in which aerosols can act as IN and how efficiently certain aerosols act as IN.

In addition to soot, other aerosols that may provide efficient IN are polycyclic aromatic hydrocarbons (PAHs). PAHs are emitted into the atmosphere through incomplete combustion of organic matter in such processes as fossil fuel and biomass burning with 90% of PAH emissions being anthropogenic in nature [*Finlayson-Pitts and Pitts, 1986*]. These organic pollutants consist of two or more benzene rings. The three and four ring compounds are semivolatile and exist in both the gas and particle (solid) phases [*Calvert, 2002; Perraudin et al., 2007a*]. The PAHs phenanthrene, anthracene, and pyrene were chosen for this study due to their abundance in the atmosphere, especially in polluted urban environments. Phenanthrene is one of the most abundant PAHs, 10 times more abundant than anthracene [*Calvert, 2002*]. The PAHs used in this study are shown in Table 1.

Table 1. List of PAHs to be used in this research. Structure images adapted from *Perraudin et al.* [2007a]

Name	Structure	Number of rings	Molecular mass (g/mol)	Purity (%)	Supplier
Phenanthrene		3	178	99	Sigma-Aldrich
Anthracene		3	178	98	Sigma-Aldrich
Pyrene		4	202	99	Sigma-Aldrich

PAHs are primarily emitted as particles less than 5 μm in diameter and have toxic effects on human health. These particle sizes are more likely to travel deep into the lungs, which results in allergenic, mutagenic, and carcinogenic effects [*Kwamena et al.*, 2006]. PAHs are found in air, water and soil near urban areas [*Kahan et al.*, 2006]. Also, since PAHs have a high affinity for carbonaceous surfaces, they may be absorbed into porous soot particles [*Bedjanian et al.*, 2010; *Lary et al.*, 1999].

Previous studies show that PAHs oxidized by gases, such as ozone, can become increasingly more toxic than their parent compounds and increasingly dangerous to human health [*Calvert*, 2002; *Finlayson-Pitts and Pitts*, 2000]. Homogeneous gas-phase reactions and heterogeneous surface reactions of PAHs, including ozone reactions with surface-bound PAHs and the consequential oxidation products, have been a topic of recent research [*Bedjanian and Nguyen*, 2010; *Finlayson-Pitts and Pitts*, 2000].

Perruadin et al. [2007] found that surface reactions on PAHs are more rapid and therefore, more relevant in the atmosphere than gas-phase reactions. PAHs in the particle phase, like those in this study, are found primarily on surfaces due to their lower volatility than PAHs in the gas phase. Hence, heterogeneous reactions, such as oxidation by ozone, are considered more important for the larger PAHs [*Kahan et al.*, 2006]. Oxidation changes PAHs at the surface; however, it is still unknown how oxidation of PAHs affects ice nucleation ability. This study investigates the chemical properties and the ice nucleation efficiency of PAHs before and after ozone oxidation.

The main goal of this study is to explore ice nucleation efficiency in experiments in which PAHs and soot are used as IN. An ice microscope apparatus is utilized to identify freezing temperatures for fresh and oxidized soot and PAHs, leading to a better understanding of ice nucleation efficiency. Another goal is to identify changes in chemical and physical properties that occur within soot and PAHs after oxidation by ozone. FTIR was used to identify chemical changes at the surface of the soot and PAHs after O₃ oxidation. Surface area measurements obtained through the BET method are compared to calculations using geometric surface area to obtain single particle nucleation rates and the likelihood of freezing. Taken together, all of these experiments will help to clarify the uncertainties that remain regarding aerosol-cloud interaction and climate change.

2. EXPERIMENTAL METHODS

2.1 Sample Preparation

Soot was chosen as one of the aerosols for this research. Carbon (Lampblack) from Fisher Scientific was chosen as a surrogate for atmospheric soot due to its availability for the duration of this research. The soot was sifted through 3 inch diameter wire mesh sieves from the Newark Wire Cloth Company to achieve three different size ranges: 250-300, 125-150, and 45-53 μm in diameter. This produced average size particles of 275, 137, and 50 μm , respectively. After the soot is sized, about 25-30 mg of the sample was separated to be oxidized. The remainder of the sample was labeled as fresh soot (unexposed to the aging process) and stored in dark glass jars.

In addition to soot, the PAHs anthracene, pyrene, and phenanthrene were chosen as IN. Solid PAH particles were sifted to 137 μm diameter and stored in glass jars. A portion of the PAHs was oxidized in the same manner as soot.

Ozone was chosen as the oxidizing trace gas because it is found in high concentrations (over 100 ppb) in the atmosphere where soot and PAH concentrations are highest, which occurs in many urban areas [*Kahan et al.*, 2006]. The sized aerosol to be oxidized was placed on a glass fiber filter (Advantec [®]) and placed inside a Nalgene chamber. Ozone flowed through a piece of tubing connected to the top of the chamber. The O₃ was obtained from a HC-30 generator (Ozone Solutions), which obtained its supply from an oxygen tank. The oxygen entered the generator at a flow rate of 0.01 liters per minute (lpm), which was controlled by a mass flow controller (Model MC-10SLPM-D(O₂), Alicat), and passed into a corona cell, where the molecular oxygen was

split into atomic oxygen, and then reacted with diatomic oxygen to form O₃. Ozone was produced at high concentrations of 3-28 grams per hour with concentrations 5-14% by weight (equivalent to 50,000 – 140,000 ppm). In order to obtain a steady ozone concentration, part of the O₃ flow (0.02-0.08 lpm) was pulled off by a pump prior to the mixing chamber and sent to the vent hood. Once the ozone entered the mixing chamber, it was diluted with nitrogen gas (N₂) at a flow rate of 10 lpm. A liquid nitrogen cylinder provided nitrogen gas, and a mass flow controller (Model MC-10SLPM-D (N₂), Alicat) controlled the flow of N₂. The mixture of O₃/N₂ gas was then directed to the vent hood where the sample in the chamber was located. Ozone concentration was measured by an UV absorption analyzer (UV-100, Eco Sensors, Inc, 254 nm). The UV analyzer drew a flow of 1 lpm from the main line prior to being sent to the vent hood. Ozone concentrations of 20 -100 ppm were generated using this method. A concentration of 80 ppm remained constant during the oxidation process, which lasted for 24 hours. The concentration of ozone varied at most ± 5 ppm throughout the experiment.

Although this concentration seems extreme when compared to typical atmospheric concentrations of 30 – 40 ppb [*Finlayson-Pitts and Pitts, 2000*], the higher concentration was chosen to ensure oxidation. Since soot remains in the atmosphere for several weeks, a high concentration of O₃ is appropriate to produce the effect of longer periods of aging in the atmosphere [*Seinfeld and Pandis, 2006*]. Ozone reactions with anthracene shorten the lifetime to a maximum of a few hours. The lifetime of phenanthrene after ozone exposure is between one hour and one day [*Perraudin et al., 2007a; b*]. At the end of the 24 hour oxidation, the sample was removed from the reaction chamber and stored in a

dark glass jar to avoid further oxidation. The oxidized samples were then used for FTIR and ice nucleation experiments. Experimental methods for all procedures are described below.

2.2 Fourier Transform Infrared Spectroscopy-Horizontal Attenuated Total Reflectance Experiments

FTIR was used to identify chemical bonds in soot and PAHs and to identify changes in the chemical composition of the surface after oxidation. Horizontal Attenuated Total Reflectance- Infrared (HATR-IR) was utilized because it was useful for observing surface changes. HATR enabled the use of infrared spectroscopy to analyze substances by simplifying sample preparation and allowing robust spectral reproducibility. The experiment used a HATR chamber (Pike Technologies) with Perkin Elmer Spectrum 100 Fourier Transform software to collect spectra. IR absorption was a result of various energy changes causing repositioning within the molecules. The HATR worked by measuring absorption that occurred in an internally reflected IR beam when the beam made contact with the sample through the crystal at a high refractive index. The transmitted energy resulting from the internally reflected IR beam exited the opposite side of the crystal where it was measured by the detector in the IR spectrometer.

A sample was placed on the Zinc Selenium (ZnSe) crystal with a refractive index of 2.4, a spectral range of 20000-630 cm^{-1} and a pH range of 5-9. Before the sample was placed on the HATR crystal, the instrument was set to a resolution of 2 cm^{-1} . Absorbance was measured over the wavenumber range of 4000 to 700 cm^{-1} . After the

parameters were chosen and the HATR plate void of any sample was placed into the chamber, a calibration was completed by collecting a background spectrum. Once the background spectrum was obtained, a sample was placed directly on the HATR plate. Previous work from *Mason* [2009] shows that the FTIR-HATR technique works best for liquids and solid films because they provide the best contact with the crystal. The background spectrum that was previously taken was subtracted from the sample spectrum as it was being collected by the software, ultimately giving the spectrum of the sample.

High quality soot spectra were difficult to obtain due to the nature of soot particles. Since the soot was a non-dissolvable solid, it shifted during the scans of the experiment, causing a large amount of noise in the spectrum. Since the loose soot particles were disrupting the absorbance measurement, olive oil was used to keep the soot in one even layer of a black oily mixture on the crystal plate. The spectrum of olive oil was subtracted from the soot plus olive oil mixture. The resulting soot spectrum looked similar to past studies [*Mason*, 2009]. This oil mixture was created using oxidized soot as well. Figure 3 shows the three spectra of olive oil, soot + olive oil, then the difference of (soot + olive oil) – olive oil, which is the resulting oxidized soot spectra. Analysis was done upon completion of the experiment to identify to which chemical bonds the peaks correspond.

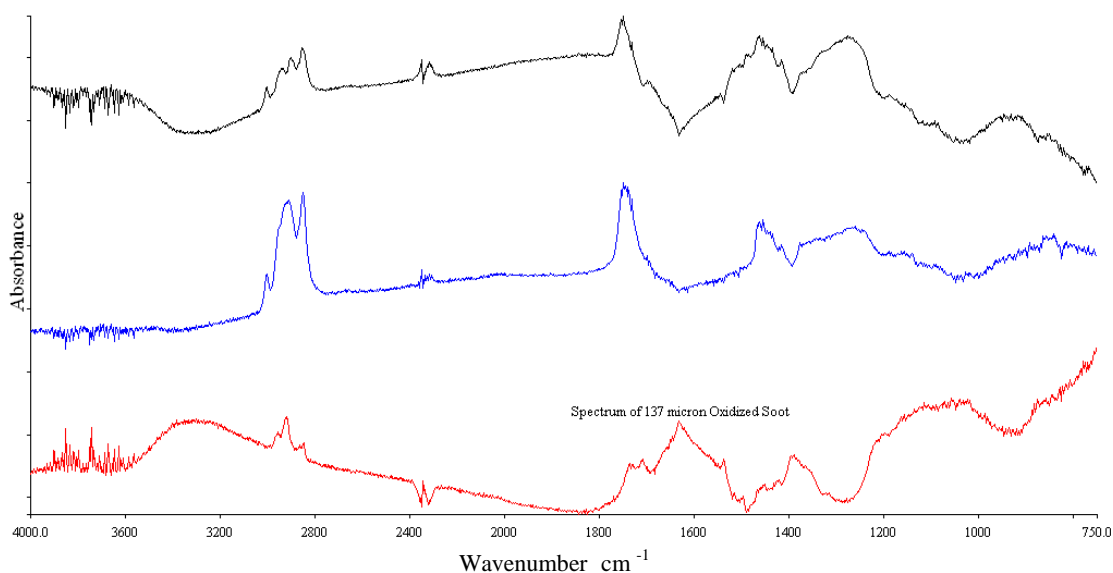


Figure 3. From top: Olive oil (black), 137 μm oxidized soot mixed with olive oil (blue), and the difference spectrum of 137 μm oxidized soot plus olive oil-olive oil (red) allows just the spectrum of 137 μm oxidized soot to remain.

Soot samples were scanned 20 times to try to reduce the noise that still remained.

Though a noisy spectrum was obtained, FTIR is still the most definitive analytical tool available to study the structure and reactivity of soot. Because PAH solid particles can be dissolved in acetone, a slightly different experimental method was used and described below.

The PAHs used in this study contain certain characteristics that are advantageous for FTIR experiments. The PAH solid particles were dissolved into solution due to their solubility in acetone. This allowed a thin film of PAH to remain on the ZnSe crystal plate when the acetone had evaporated, which allowed a better spectrum to be obtained [Hung *et al.*, 2005]. Mason [2009] tested different mixtures of PAH/acetone to determine the smallest amount of PAH that would give a clear spectrum. Ultimately, a concentration of 1 mg of PAH for every 1 ml of acetone for all the PAH solutions was

chosen because it allowed for the lowest number of monolayers, yet still allowed a strong enough substance signal so that molecular bonds could be identified. This method was used for PAH measurements in this research. After adding a ratio of 1 mg of PAH to 1 ml of acetone, the solution was stirred for 20 minutes to allow all the PAH to dissolve completely in the acetone. Once the solution was ready, fifty microliters were placed on the crystal plate. To ensure the acetone had evaporated, the sample was placed in the HATR chamber for at least 30 minutes. After monitoring the spectra using the Timebase software, it was confirmed that acetone evaporates rapidly (less than 30 minutes). Previous spectra of acetone were used for reference to ensure that no acetone remained once the experiment began. *Mason* [2009] also determined that the acetone did not chemically alter the PAHs and that the HATR spectra resembled the transmission spectra.

2.3 Ice Nucleation Efficiency Experiments

In order to study the soot and PAH samples as IN, ice efficiency experiments were performed using a microscope with an attached digital camera and Teflon coated cooling stage. Previous colleagues formulated a method that allowed a distinction to be made between immersion and contact freezing [*Fornea et al.*, 2009; *Fornea*, 2009]. The original idea to explore heterogeneous freezing of any ice nucleus using this technique was presented in *Durant and Shaw* [2005]. Their study utilized an apparatus that allowed the study of contact and immersion freezing using a number of heating and cooling cycles [*Durant and Shaw*, 2005]. A droplet containing an ice nucleus was frozen,

melted, and then refrozen many times in one experiment. This was done so numerous data points were taken from the same aerosol and droplet, limiting the possible variables in the experiment [Durant and Shaw, 2005; Shaw *et al.*, 2005]. Because ice nucleation is a stochastic process, obtaining multiple data points with the same IN is advantageous. The experimental design for this study is based on that of Durant and Shaw [2005].

In order to study two forms of heterogeneous freezing (contact and immersion) ice nucleation efficiency experiments were performed using a microscope apparatus. Figure 4 shows the experimental design developed by Fornea *et al.* [2009], which was used for this study. Using this apparatus, ice nucleation was observed, and the freezing temperature was recorded.

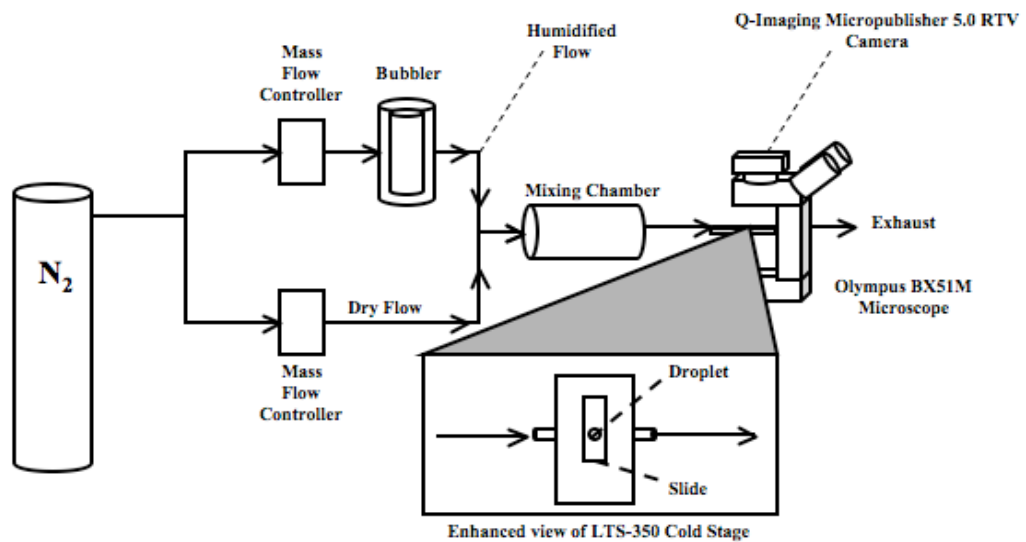


Figure 4. Experimental design of ice microscope. Adapted from Fornea *et al.* [2009].

The experiment began with a tank of dry nitrogen gas flowing into a Nalgene bubbler, creating a low humidified flow. This flow was used to prevent droplets on the cooling stage of the microscope from evaporating: the humidified flow contained 0.57 lpm of dry nitrogen flow and 0.03 lpm humidified flow, controlled separately by mass flow controllers (Model MC-10SLPM-D (N₂)). The two flows continued through a mixing chamber to create a total flow rate of 0.60 lpm before entering the cold stage (Model LTS-350, Linkam). A dewpoint hygrometer (Model 2000 series DewPrime II, EdgeTech) measured the dewpoint of the total flow prior to entry into the cold stage. Even with some humidified flow, there was no detectable condensation growth of the droplet itself. To prevent condensation on the 0.8 mm microscope slides (VWR), they were silanized with a 2.0% Aquasil solution (Pierce Chemical Company) producing a hydrophobic surface. The temperature of the slide was controlled to within a tenth of a degree. The cold stage was a sealed chamber, which was connected to a temperature controller box and a liquid nitrogen pump that were used during the heating and cooling cycles. The cold stage and temperature controller box were both controlled by Linksys 32 software (Model Linksys 32-DV, Linkam). The stage was attached to an optical microscope (BX51M, Olympus) equipped with a digital camera (Micropublisher 5.0 RTV, Q-Imaging) looking down on the slide. This experimental design allowed the droplet with the ice nucleus to be monitored throughout the experiment cycles. Images taken by the digital camera were viewed during the experiment using the Linksys 32 software. An image was captured every six seconds, which means an image was taken every tenth of a degree. In the final stage of experimental preparation, a sample was

prepared outside the cold stage. A 2 microliter droplet of ultra pure (HPLC grade) water was placed on a slide with a hydrophobic (silanized) coating. The volume of the droplet was measured using an Eppendorf micropipettor. Then the ice nucleus was placed in contact with the water droplet. Once the microscope slide containing the droplet and ice nucleus was sealed inside the cold stage, which had been cooled to 5 °C, the experiment began. In the experiment, the temperature of the stage was controlled to run through the following cycle repeatedly. The cycle began at 5 °C decreasing to -40 °C at a rate of 1 °C/min. Once -40 °C was reached, the stage automatically warmed at a rate of 10 °C/min until it reached 5 °C, where it remained for one minute to ensure the droplet had fully melted.

A rate of 1°C/min was chosen for this experiment. Previous work provided empirical testing to show that this was a reliable rate. In addition, a simple calculation shows why 1°C/min is slow enough to capture the freezing event. By using the diffusion equation, it is seen that the timescale on which freezing occurs is far greater than the time it takes the droplet to adjust to the ambient temperature.

$$\frac{\partial T}{\partial t} = \mu \frac{\partial^2 T}{\partial x^2} \quad (1)$$

The diffusion equation involves a change in temperature over a change in time. If solving for time, one needs to square the diameter of the object in question, and divide by the thermal diffusivity constant μ . Considering the volume of the droplet is 2 μL (0.002 cm^3), this equals a diameter of 0.16 cm using the equation for volume of a sphere. The thermal diffusivity value for ice and water was discussed in past literature and was

found to be $12.5 \times 10^{-3} \text{ cm}^2\text{sec}^{-1}$ at $-40 \text{ }^\circ\text{C}$ and $1.35 \times 10^{-3} \text{ cm}^2\text{sec}^{-1}$ at $0 \text{ }^\circ\text{C}$ [*James, 1968*].

Squaring the diameter and inserting one of these values for μ leads to a small timescale in which diffusion occurs. The value is on the order of 2 seconds for ice. A freezing event takes a few seconds from initiation of freezing to the droplet completely freezing, meaning that a small value of diffusion ensures that the $1 \text{ }^\circ\text{C}/\text{min}$ rate is substantially slow enough to not miss any important data.

The number of repetitions for each experiment was about 33 cycles, resulting in 33 individual freezing events. The saved images were analyzed to determine at what temperature a freezing event had occurred upon completion of the experiment. A freezing event was identified through a change in reflectivity, as the sample changed from a transparent droplet to a solid ice crystal. In addition, at the time of freezing, a wave of motion throughout the droplet was usually seen.

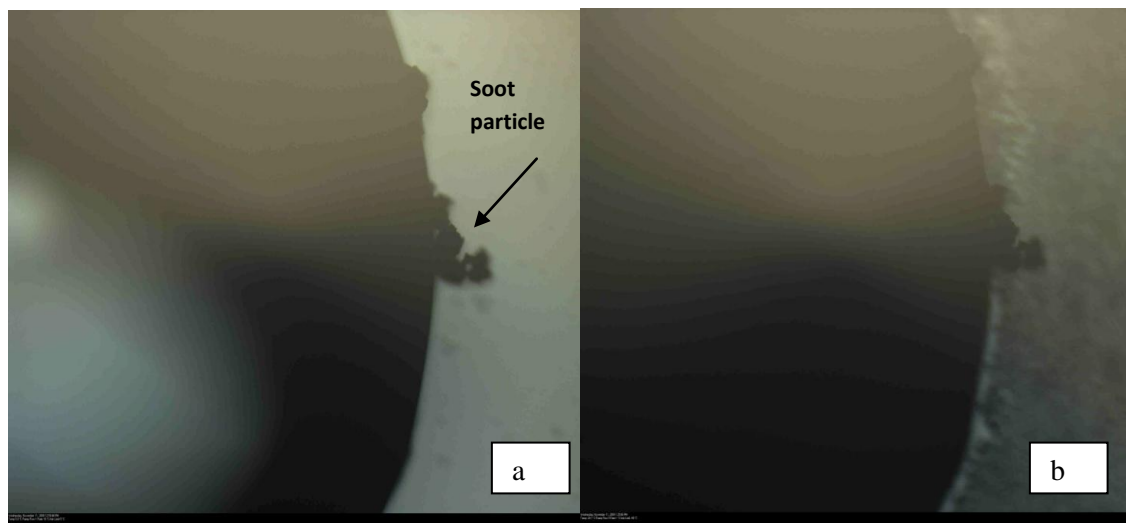


Figure 5. Unfrozen (a) and frozen (b) droplet with fresh soot acting as IN for contact freezing. The soot particle is seen on the right hand side of the droplet. The disappearance of the reflective (white) area implies the droplet has frozen.

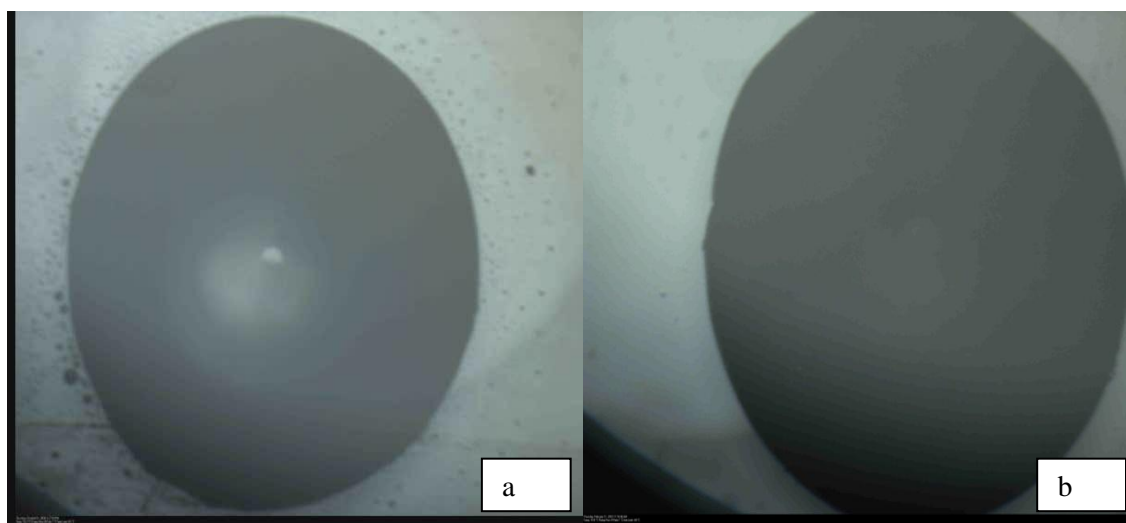


Figure 6. Unfrozen (a) and frozen (b) droplet with oxidized soot acting as IN for immersion freezing. The soot particle is inside the water droplet. The disappearance of the reflective (white) center and the change to an opaque droplet implies the droplet is frozen.

Figure 5 shows an unfrozen (a) and frozen (b) droplet for fresh soot, and Figure 6 shows an unfrozen (a) and frozen (b) droplet for oxidized soot. By analyzing this experiment in frames, accurate identification of the freezing event and recording of the freezing temperature was possible. Each experiment gave a sequence of freezing temperature data with one temperature for each cycle. Experiments differed in the amount of variability in this sequence. Figure 7 shows one experiment that used an oxidized soot sample of $137\ \mu\text{m}$ diameter where little variation in freezing temperature occurred (the standard deviation was $0.66\ ^\circ\text{C}$).

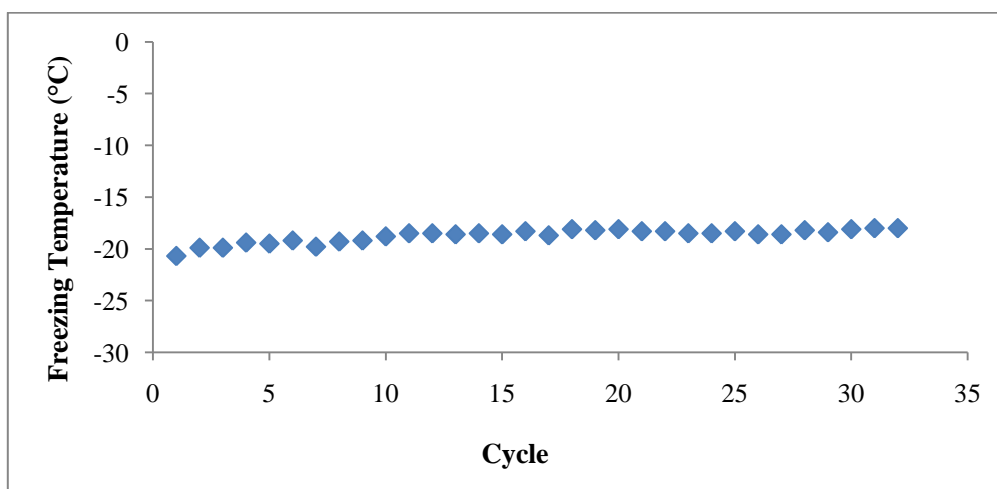


Figure 7. One experiment ($137\ \mu\text{m}$ oxidized soot) containing 33 cycles where there is little variability.

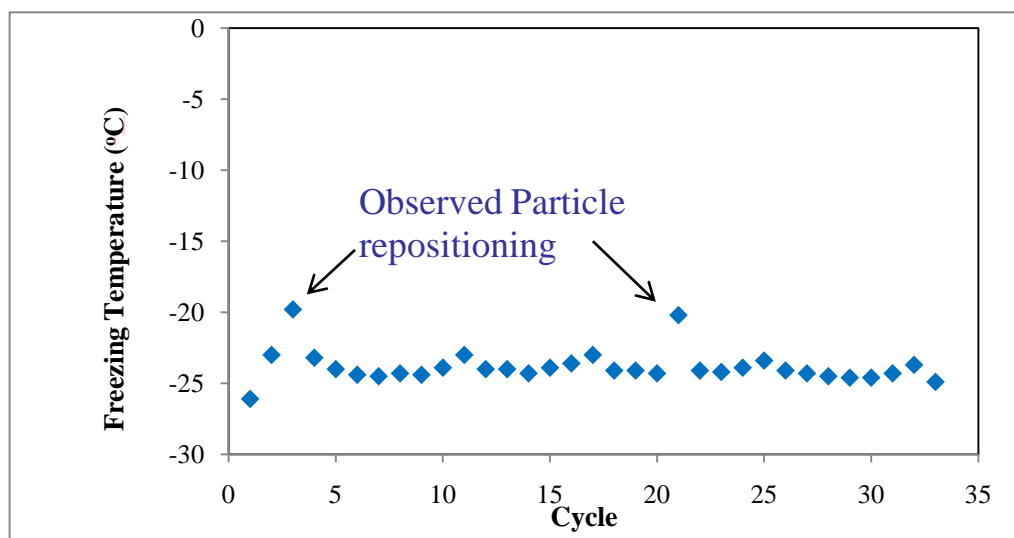


Figure 8. Variability within one experiment (fresh 50 μm soot) is seen due to possible particle repositioning.

Data from a fresh soot experiment are shown in Figure 8, where there is much greater variability (the standard deviation was 1.16 $^{\circ}\text{C}$). The variability may be due to occasional movement of the soot particle seen during melting and freezing. Variability from one experiment to the next may be due to the intrinsic properties of the IN and that freezing is a stochastic process [Vali, 2008]. Although the observed variability is not well understood, similar behavior was previously reported by Vali (2008). Further discussion of randomness and variability is given in the results section.

The PAH samples were used in the same experimental method as soot for ice nucleation experiments. Certain characteristics of the selected PAHs for this study were advantageous for ice nucleation experiments. The chosen PAHs were all insoluble in

water. The insolubility in water was a useful property for ice efficiency experiments because when a PAH solid particle was placed in contact with the water droplet, the PAH sample did not dissolve, providing more accurate data measurements. The freezing mechanism depended on the composition of the IN. The behavior of PAHS as IN depended on which composition was used. When a fresh or oxidized anthracene particle was introduced to the water droplet, it remained in contact with the surface for the length of the experiment. The clear color of the solid PAH samples made it difficult to observe the placement in reference to the water droplet. However, it was evident that the PAH particle did not stay outside the droplet like a hydrophobic fresh soot particle would. Also, there was little movement of the anthracene particle throughout the experiment. Phenanthrene particles acted differently than anthracene. Fresh phenanthrene remained in contact with the surface, but oxidized phenanthrene had differing freezing mechanism throughout the experimental runs. Some oxidized phenanthrene experiments began as contact freezing and ended as immersion. The particle moved during some, but not all, experiments using oxidized phenanthrene as IN. These shifts may be due to the intrinsic properties of the IN as proposed for the soot particles. The immersed oxidized phenanthrene particle, however, did not break up like the oxidized soot did, and the IN particle remained intact throughout the experiment. Fresh particles of pyrene remained in contact with the water droplet. Oxidized pyrene immediately immersed into the water droplet upon introduction to the side or top of the droplet. The oxidized pyrene crystal also remained in one piece for the duration of the experiment. Overall, the behavior of the IN and the freezing temperature depends strongly on the composition. No previous

literature is available using PAHs as IN; consequently no known freezing temperatures are available for comparison.

2.4 Brunauer-Emmett-Teller (BET) Method

Ice nucleation rates depend on surface area measurements. For porous materials such as soot, the specific surface area is a more accurate measure than geometric surface area. A study by *Aubin and Abbatt* [2003] found that the BET specific surface area for soot was 88-372 times larger than the calculated geometric surface area. The specific surface area of soot was measured by adsorption using the Brunauer-Emmett-Teller (BET) method. Surface area measurements were obtained to determine if any differences occur between the three sifted sizes of soot and between fresh and oxidized soot. Specific surface area is defined as the total surface area per unit mass. The equation used for the calculation of geometric surface area for a sphere is $4\pi r^2$, where the radius, r , is half of the diameter of the sphere. The diameter for soot in this study was obtained by taking the average of the range possible for the given sieve (i.e. the 250-300 μm sieve has an average diameter of 275 μm).

The BET method is appropriate when multilayer adsorption is possible, leading to each layer of gas adsorbed independently. The BET theory uses an extension of the Langmuir model, which is limited to monolayer adsorption, to include multilayer adsorption [*Brunauer et al.*, 1938]. Therefore, the following assumptions are made (1) each molecule adsorbed in a particular layer is a possible site for adsorption of a molecule in the next layer, (2) no horizontal interactions occur between adsorbed

molecules, (3) the heat of adsorption is the same for all molecules in any given adsorbed layer, and (4) the heat of adsorption is equal to the latent heat of evaporation for all adsorbed layers except the first one [Popovicheva *et al.*, 2008b]. The BET method was used to create an adsorption isotherm at 77 K [Levitt *et al.*, 2007]. The BET isotherm was developed by Brunauer, Emmett, and Teller to include multilayer adsorption, ultimately leading to condensation of the vapor as a liquid onto a solid [Hunter, 1993]. Research purity Krypton (Kr) from the Matheson Tri-Gas Company was chosen as the gaseous species due to its lower saturation vapor pressure [Yanazawa *et al.*, 2000]. In this study, a Kr adsorption apparatus was utilized in collaboration with Dr. Renyi Zhang to obtain a BET isotherm from which specific surface area would be calculated. Because soot is a porous material, multiple layers condense on the surface and how these layers form dictate the shape of the BET isotherm. The surface area in square meters per gram was calculated using the BET isotherm [Brunauer *et al.*, 1938]. A 15-30 mg sample of monodispersed soot, fresh or oxidized, was placed in a foil cylinder tube with one end open inside a custom-made glass flask with one inlet. The flask was then sealed with a vacuum jacket and was connected to the vacuum manifold. The pressure was obtained using a Fluke multimeter. Once the pressure equaled zero torr, the experiment began. A liquid nitrogen tube was placed on the outside of the sample tube to keep it at thermal equilibrium. After thermal equilibrium was reached, the dead space volume inside the sample tube was measured using Helium (He). The He calibration was performed until an adequate amount of points were taken. The data were then put into the Kr adsorption equation to calculate the BET surface area. After all the He had been evacuated from the

sample tube, Kr adsorption began by allowing some pressure level of Kr to be admitted into the sample tube. The experiment usually began with Kr levels of 1 torr. The operation was completed once the desired pressure range was covered [Rosenberg, 1956]. In each Kr adsorption, pressure needed to remain constant for a couple minutes after Kr was introduced. A reading was taken 5 minutes after Kr introduction to the sample, similar to the procedure described in Yanazawa *et al.* [2000].

Using this experimental method it was possible to calculate the amount of Kr adsorbed by the soot surface from the known amount of Kr added, the known total volume of the system, and the change in pressures [Levitt *et al.*, 2007]. The uptake of Kr and the surface area are described by the BET equation [Gregg *et al.*, 1967].

$$\frac{P}{V(P_0 - P)} = \frac{1}{V_m C} + \frac{P(C-1)}{V_m C P_0} \quad (2)$$

where P_0 is the saturation vapor pressure of the Kr, V is the adsorbed volume in units of cubic centimeters at standard temperature and pressure (STP), V_m is the volume of the monolayer capacity also at STP, and C is the dimensionless BET constant [Levitt *et al.*, 2007]. Manipulation of this equation allowed $P/[V(P_0 - P)]$ to be plotted against P/P_0 , yielding a linear relationship within the range 0.05-0.5, similar to the method used by Aubin and Abbatt [2003]. Using a linear fit of this plot, the linearized BET isotherm was obtained. From here the BET surface area (SA_{BET}) of the soot was calculated by

$$SA_{\text{BET}} = V_m N_A \sigma_{\text{Kr}} \quad (3)$$

Here, V_m is the monolayer capacity converted to moles, N_A is Avogadro's number, and σ_{Kr} is the atomic cross-sectional area of Kr [Levitt *et al.*, 2007]. This equation gives the specific surface area for each sample using the isotherms produced.

Figure 9 is an example of the BET isotherm. Due to large Kr uptake, the pressure eventually reached its limiting value near 0.69, which is the vapor pressure of solid Kr at 77 K [Rosenberg, 1956]. At the last point on the graph near 0.800, the equilibrium vapor pressure had been reached for the condensed liquid. This was seen by the adsorption exponentially increasing and forming a macroscopic film of liquid Kr on the soot surface [Hunter, 1993]. The vertical line due to no P/P_0 change seen in Figure 9 demonstrated the completion of this film. This is indicative of a Type 2 isotherm, which is seen when physical adsorption occurs with multilayer formation [Aubin and Abbatt, 2003; Brunauer *et al.*, 1938]. Figure 9 begins at Point B where the first monolayer is completed, and multilayer adsorption can commence [Aubin and Abbatt, 2003; Brunauer *et al.*, 1938]. This graph gives the number of moles required to form the monolayer and the cross-sectional area of the adsorbate gas, so the BET surface area can be calculated by Equation 3. Using the linear form of the BET equation, a graph (Figure 10) was plotted for P/P_0 vs. $P/[V(P_0-P)]$. The beginning of the linear portion starts at Point B, around 0.1 and ends at 0.5 [Brunauer *et al.*, 1938].

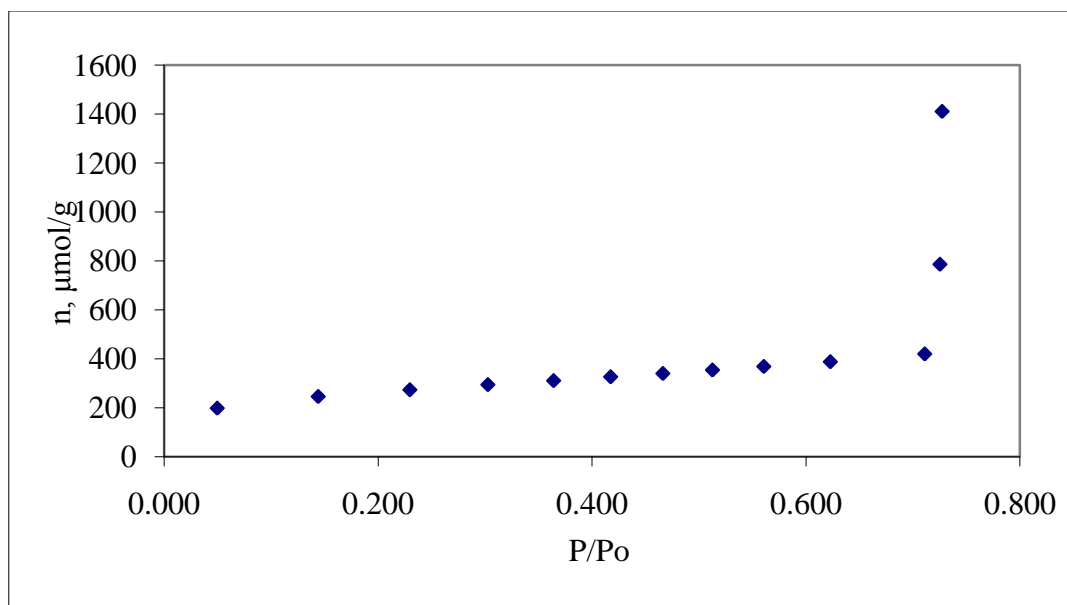


Figure 9. Adsorption isotherm of Kr on fresh 45-53 μm lampblack soot.

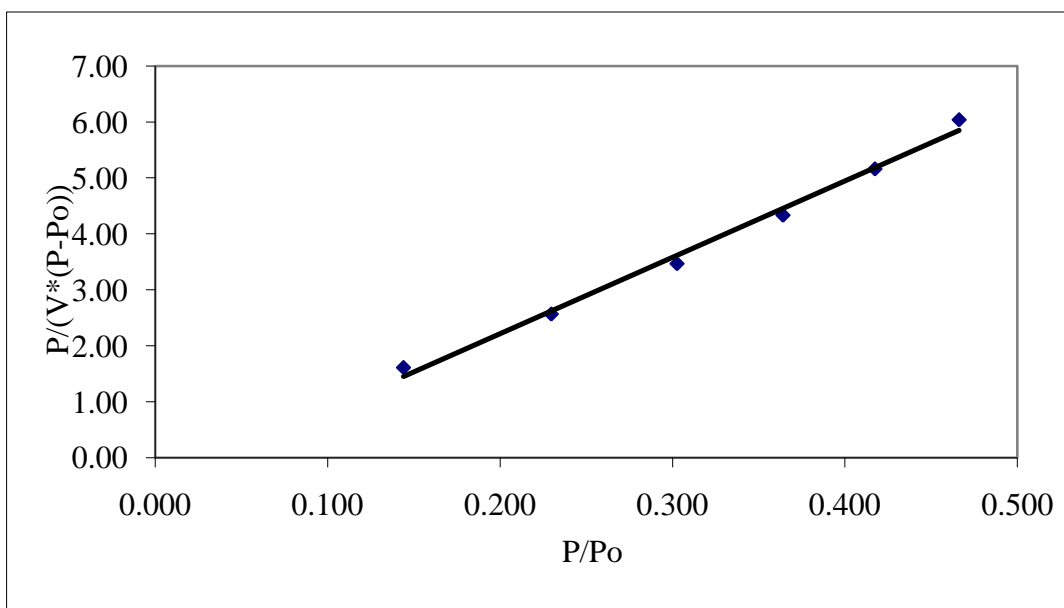


Figure 10. Linearized form of the BET isotherm for the adsorption of Kr on 0.019 g of 45-53 μm fresh lampblack soot. $R^2 = 0.9925$ showing this is a good linear fit.

From these two graphs, all variables for Equation 3 were obtained, and the outcome was the specific surface area. According to previous literature, the specific surface area for Lampblack soot is $22 \text{ m}^2/\text{g}$ [Popovicheva *et al.*, 2008a]. In this study, the BET method was performed on samples of fresh and oxidized soot for each of the three sizes. Experiments using fresh soot were run twice with different samples, equaling 6 total experiments. For oxidized samples of each size, only one run was performed per sample due to lack of variability. This provided specific surface area values for each size of fresh and oxidized soot. Based on the above experimental method and equations used, the BET surface area measurements have an accuracy of $\pm 10\%$ [Yanazawa *et al.*, 2000].

3. RESULTS AND DISCUSSION

3.1 FTIR Results

FTIR spectra were obtained to compare fresh and oxidized samples of soot and PAHs. Analysis of the spectra showed that new peaks formed, verifying that the samples were oxidized by ozone. FTIR reveals the chemical changes that occurred on the sample surface due to oxidation. Ozone destroyed the carbon bonds of the soot and PAHs, and also caused new bonds to form. All oxidized samples formed a C=O bond. PAHs also formed new C-O, O-H, and C-H bonds. The presence of these chemical bonds was a result of the formation of carboxylic acids and aldehydes on the surface of the oxidized sample. These chemical changes lead to a change in hygroscopicity, which affect the IN ability of the samples. Therefore, FTIR spectra are an important tool in determining how oxidation leads to changes in IN efficiency.

3.1.1 FTIR Results for PAHs

After spectra for fresh and oxidized samples of PAHs and soot were taken by the FTIR, the spectra were analyzed to identify chemical bonds. Figures 11a, 11b, and 11c show the spectrum for each fresh PAH chosen for this study. All PAHs in this study have a peak near 3000 cm^{-1} due to their aromatic ring structure containing a C-H bond. Other peaks show C=C bonds near $1500\text{-}1600\text{ cm}^{-1}$ for aromatic rings.

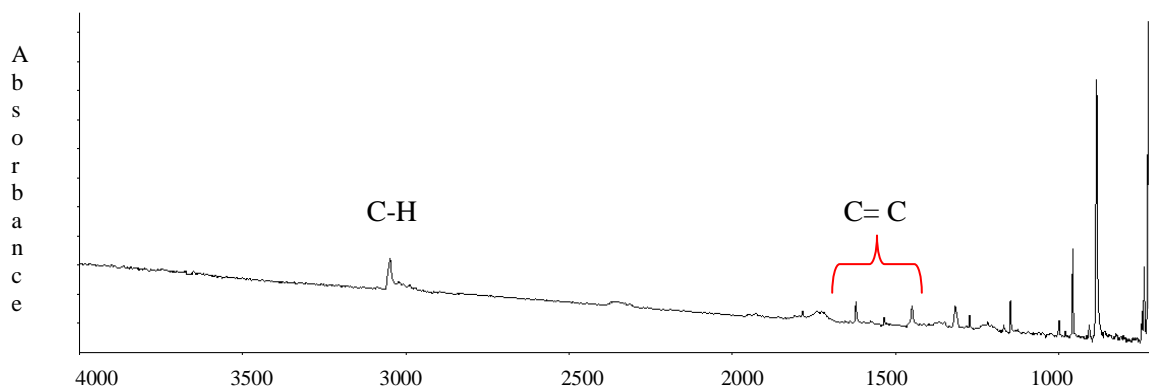


Figure 11a. Fresh Anthracene spectrum (cm^{-1}).

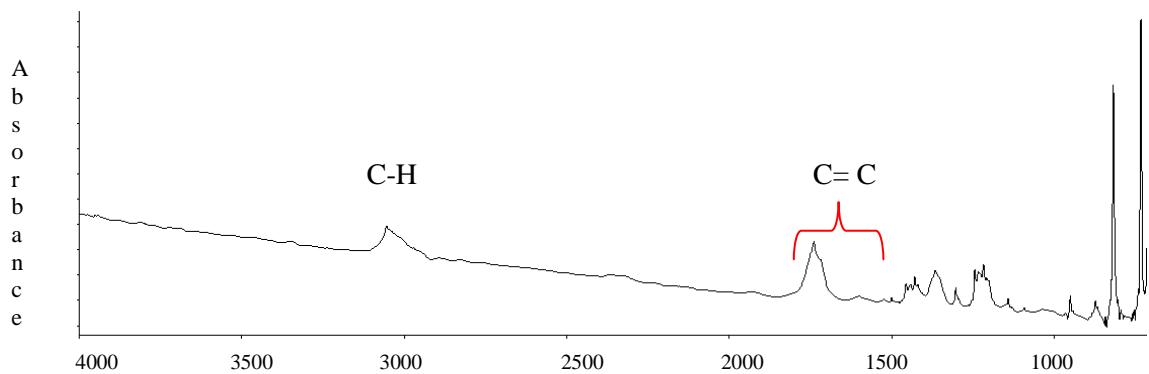


Figure 11b. Fresh Phenanthrene spectrum (cm^{-1}).

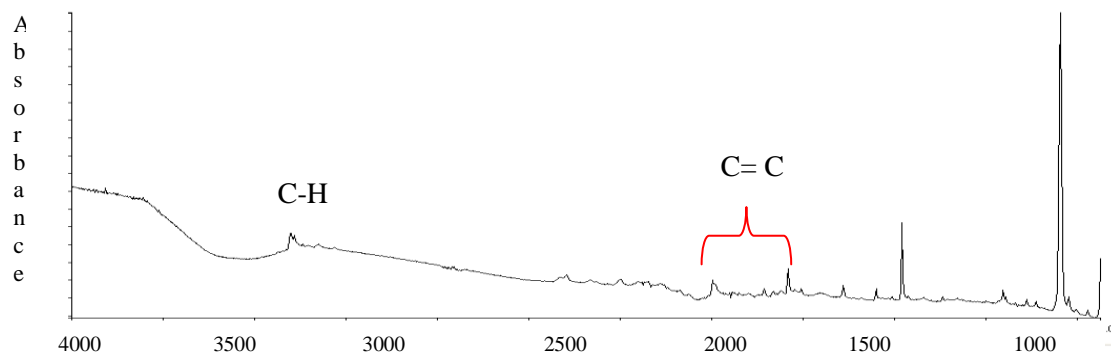


Figure 11c. Fresh Pyrene Spectrum (cm^{-1}).

FTIR was used to monitor composition changes occurring in the PAH samples due to exposure to O_3 . After exposure to ozone for 24 hours, a spectrum of an oxidized PAH sample was taken in order to observe changes that occurred on the surface and to identify any new bonds formed. The original PAH spectrum was subtracted from the oxidized PAH spectrum to show the alterations due to ozone. The oxidized spectra for all three PAHs studied in this research show the formation of a C=O bond, indicating that carboxylic acids and/or aldehydes were formed on the surface due to ozone reacting with the PAHs. The new compounds are believed to be responsible for increasing water uptake on the surface of the PAHs, increasing their hygroscopicity.

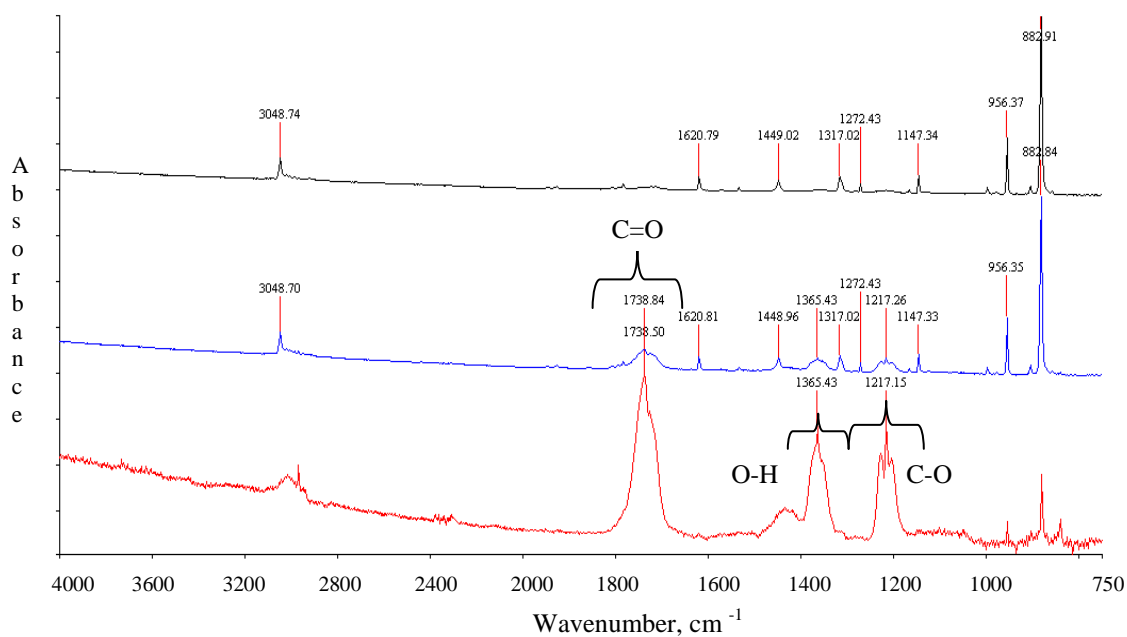


Figure 12. Fresh (black), oxidized (blue), and the difference spectrum of oxidized-fresh (red) of anthracene show new bonds formed after ozone exposure.

Figure 12 illustrates the fresh, oxidized, and difference spectrum for anthracene. Ozone oxidation causes changes at the surface of the anthracene. The peak at 1738 cm^{-1} represents the new C=O bond formed, the peak at 1365 cm^{-1} represents a bending O-H bond, and 1217 cm^{-1} peak represents a C-O stretch. This combination of bonds implies a carboxylic acid has formed at the surface of anthracene after oxidation. This agrees with previous studies that observed the formation of carboxylic acid on the surface of anthracene and other PAHs after oxidation with ozone [*Chughtai et al.*, 1991]. The formation of carboxylic acids provides a surface on which water could adhere, which could possibly improve the water uptake ability. The growth of the C=O peak is due to the three oxygen molecules of ozone attaching to the carbon of the PAHs. The location of this bond on the molecule determines the name of the oxidation product. For example, the two known ozone oxidation products of anthracene are anthraquinone and anthrone [*Perraudin et al.*, 2007a]. Anthraquinone is identified by the addition of two C=O bonds to anthracene due to bond attack by ozone at carbon 9 and 10. Anthrone results in the addition of one C=O bond. In this study, a C=O peak was present in the FTIR spectrum of anthracene, which suggests that these oxidation products found in *Perraudin et al.* [2007b] were formed.

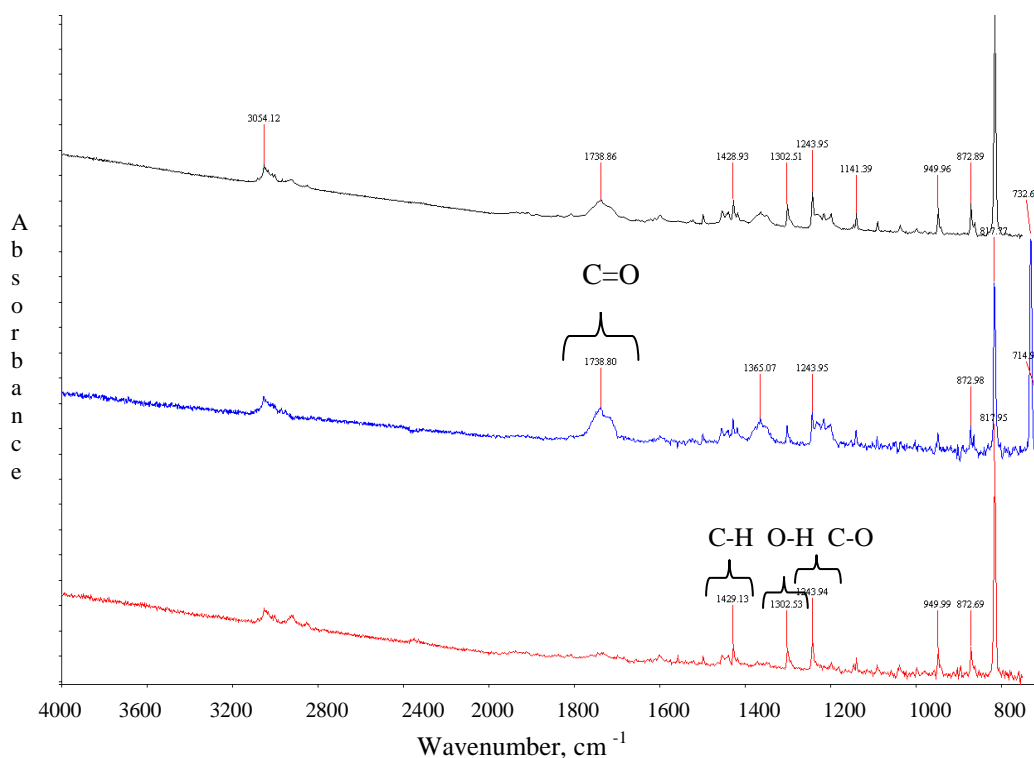


Figure 13. Fresh (black), oxidized (blue), and the difference spectrum of oxidized-fresh (red) of phenanthrene show new bonds formed after ozone exposure.

Figure 13 shows how phenanthrene changes after exposure to ozone. *Perraudin et al.* [2007b] found carboxylic acids and aldehydes to be oxidation products of phenanthrene. This is seen also in our spectra where there is growth in the oxidized spectrum near 1738 cm^{-1} showing a C=O bond. Additional new bonds were formed with a peak at 1429 cm^{-1} indicating a C-H bond, 1302 cm^{-1} indicating an O-H bond, and a peak at 1244 cm^{-1} indicating a C-O bond formed. It is well known that oxidation by ozone of a C-C bond will lead to the formation of two aldehydes, which includes a C-H bond [*Perraudin et al.*, 2007a]. The outlined mechanism for phenanthrene's reaction with ozone in

Perraudin et al. [2007b] shows the formation of C=O, O-H, and C-H bonds. This verifies that the oxidation in this study reached similar results.

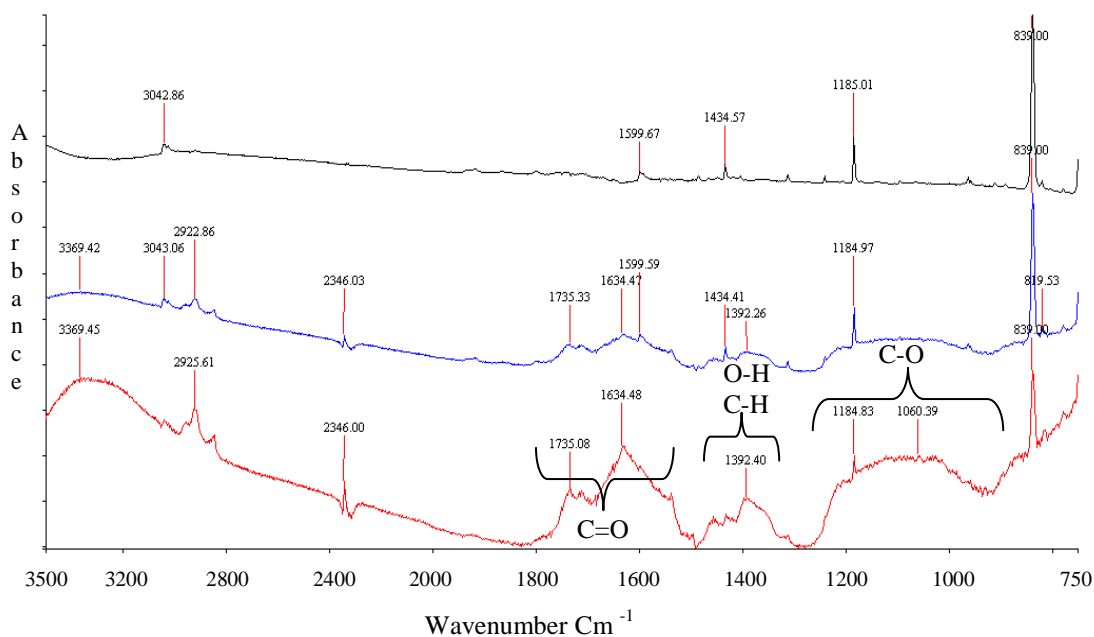


Figure 14. Fresh (black), oxidized (blue), and the difference spectrum of oxidized-fresh (red) of pyrene show new bonds formed after ozone exposure.

Figure 14 shows changes that occurred on the surface of pyrene after 24 hour exposure to ozone. The peaks at 1735 and 1634 cm^{-1} corresponds to a C=O bond, the peak at 1392 cm^{-1} indicates a O-H and C-H bond, and the broad peak from 1200 to 1000 cm^{-1} indicates a C-O stretch. This indicates an aldehyde and carboxylic acid has formed due to oxidation. *Yao et al.* [1998] identified the same oxidation products through use of gas chromatography-mass spectrometry. This verifies pyrene was oxidized by ozone, changing the chemical bonds at the surface.

A C=O bond formed on the surface of anthracene, phenanthrene, and pyrene after oxidation by ozone. To quantify this peak, the area under the C=O peak is calculated using the spectrum software. The C=O peak is located between 1600 and 1800 cm^{-1} peak though the exact center is slightly different for each PAH. The C=O peak for anthracene is centered at 1738 cm^{-1} with the beginning position of 1800 cm^{-1} and an ending position at 1650 cm^{-1} . For contrast, the area was taken at the same location for the fresh spectrum and then compared to the area under the peak for the oxidized spectrum. For anthracene, the area was equal to 0.11 absorption units for the fresh spectrum and 0.76 absorption units for the oxidized spectrum. For phenanthrene, the center of the peak is located at 1738 cm^{-1} with an area for the oxidized spectrum of 0.47 absorption units. For pyrene, there is a double peak associated with the C=O bond. This area was taken from 1800 to 1500 cm^{-1} and equaled 6.0 absorption units for the oxidized spectrum. The larger area under the C=O peak illustrates the growth of this bond after oxidation, implying a chemical change at the surface.

3.1.2 FTIR Results for Soot

The resulting spectra for soot samples were slightly more challenging to analyze due to the increased noise despite using the soot and olive oil mixture on the crystal plate. Figure 15 illustrates the difference spectra showing fresh 275 μm soot and oxidized 137 μm soot. There is no difference in spectra between sizes of soot. This is most likely due to lack of chemical change occurring from sifting to a different physical size. Despite the noise in the spectrum, a broad C=O peak has grown between 1550 and 1700 cm^{-1} . A

broad C-O peak near 1060 cm^{-1} can also be seen on the spectrum for oxidized soot. The area under the C=O curve was measured for both fresh and oxidized soot. The calculated area for the fresh soot spectrum from $1600\text{-}1800\text{ cm}^{-1}$ is 1.3 absorption units, while the area for the same peak in the same range for the oxidized soot spectra is 6.2 absorption units. The growth in the C=O peak verifies that carboxylic acids formed on the surface of the soot due to oxidation by ozone. This leads to a change from hydrophobic to hydrophilic soot particles, resulting in a change in behavior as IN.

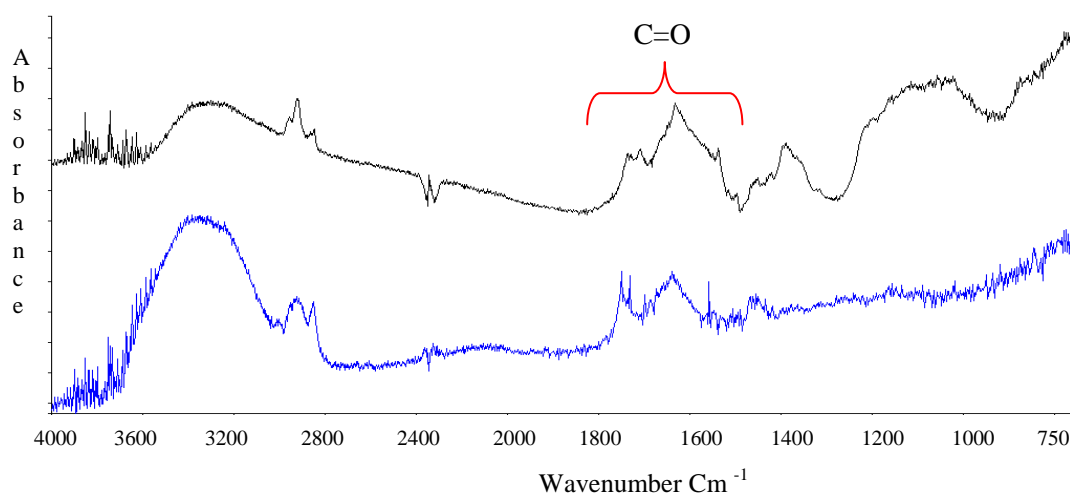


Figure 15. Oxidized $137\text{ }\mu\text{m}$ soot (black) and fresh $275\text{ }\mu\text{m}$ soot (blue) shows growth of C=O bond between $1600\text{ and }1800\text{ cm}^{-1}$ after ozone exposure.

3.2 Calibration of the Cold Stage

Former members of our research group, who are responsible for the design of the ice microscope apparatus, took precautions to ensure the accuracy of ice nucleation experiments. *Fornea et al.* [2009] describes an evaporation experiment performed with the humidified flow turned off. Figure 16 shows that though the droplet is evaporating and the experiment ends due to complete evaporation, variation within the experiment is no different than an experiment performed with humidified flow. Furthermore, this result indicates that the freezing results are not sensitive to droplet size, as the droplet becomes smaller as evaporation occurs.

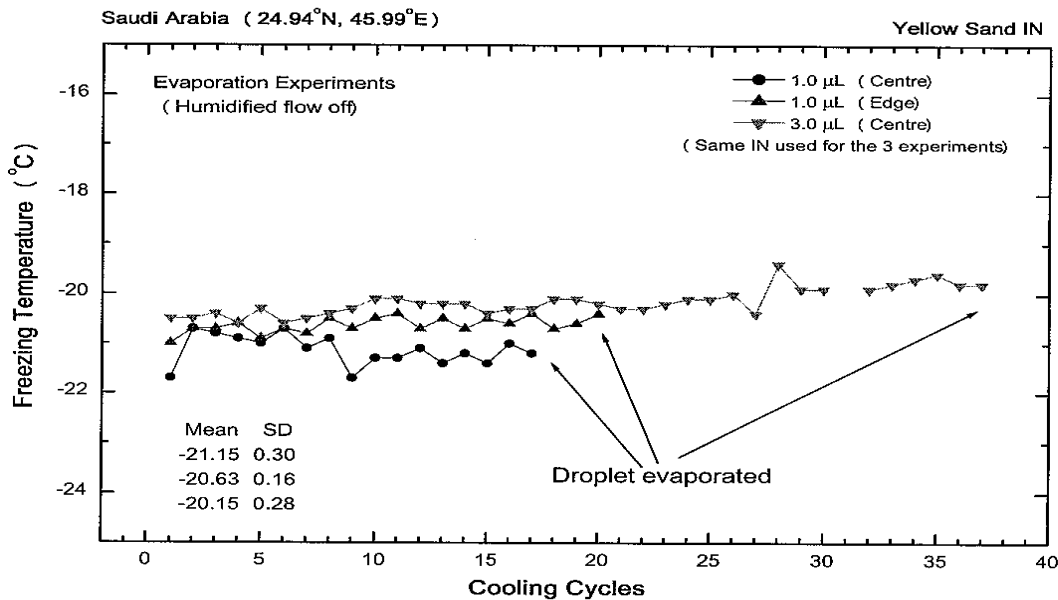


Figure 16. Using yellow sand as the IN, the humidified flow was turned off allowing the experiment to run until evaporation. This graph shows a similar mean temperature with small standard deviation even though the droplet evaporated anywhere from 20 to 35 cycles. This also shows that no matter if the droplet is 1 or 3 microliters the freezing temperature is not affected. *Brooks group*

Calibration of the cold stage was completed to ensure the accuracy of freezing temperatures. The melting point of mercury was chosen because it is a well-documented $-38.83\text{ }^{\circ}\text{C}$, which is near the coldest end of the temperature range for our experiments. A mercury droplet was frozen and melted by cyclically changing the temperature from $-60\text{ }^{\circ}\text{C}$ to $-30\text{ }^{\circ}\text{C}$ at a rate of $10\text{ }^{\circ}\text{C}/\text{min}$. An image was captured every second during this process. After three experiments using separate mercury droplets, the results showed that the average melting temperature was $-38.9\text{ }^{\circ}\text{C}$ with a standard deviation of 0.2. Previously, *Fornea et al.* [2009] observed a melting point of $-39.1\text{ }^{\circ}\text{C}$ with a standard deviation of less than 0.1 degree. This assures that both past and present experiments contain accurate freezing temperature results. Previous results showed the cold stage produced a colder melting point by about $0.3\text{ }^{\circ}\text{C}$, while current mercury experiments show a $0.1\text{ }^{\circ}\text{C}$ colder melting point.

In addition to mercury, *Fornea et al.* [2009] completed a pure water experiment to verify the accuracy of the cold stage. A HPLC grade water droplet with no IN froze at a temperature of $-33.1\text{ }^{\circ}\text{C}$ with a standard deviation of $0.6\text{ }^{\circ}\text{C}$, which corresponds with freezing temperatures observed in literature [*Langham and Mason*, 1958]. From mercury and pure water experiments, a temperature uncertainty of $0.2\text{ }^{\circ}\text{C}$ and an uncertainty due to human error in analyzing freezing events in the images of $0.1\text{ }^{\circ}\text{C}$ were determined. Therefore with this experimental design, a maximum uncertainty of $\pm 0.3\text{ }^{\circ}\text{C}$ was calculated by taking the square root of the sum of the squares of each individual uncertainty.

3.3 Results of Fresh and Oxidized Soot as IN

The chemical and physical properties of an ice nucleus determine how it interacts with the water droplet. Fresh and oxidized soot particles exhibited a preferred location on the droplet where they would naturally settle. This is important because the arrangement of the IN with respect to the water droplet governs which freezing mechanism occurs. Fresh soot is hydrophobic; so when a particle of fresh soot is placed near the water droplet, it does not go inside. Instead, the fresh soot remains at the surface due to the contact angle between the fresh soot particle and the droplet minimizing. The soot remains in contact with the droplet surface during each experiment, though some minor repositioning may be seen. Therefore, the ice nucleation ability of fresh soot has only been observed using the contact freezing mechanism.

Oxidized soot interacts with the water droplet differently than fresh soot. When an oxidized soot particle is introduced to either the side or the top of the droplet, the soot is taken into the droplet. It is not possible to position the IN adjacent to the outer surface of the droplet. In this case, the soot particle is immersed into the water droplet, allowing immersion freezing to occur. Oxidized soot behaves differently than fresh soot possibly due to the change in hygroscopicity. The formation of carboxylic acid groups makes the oxidized soot hydrophilic, causing the droplet to freeze at a warmer temperature than fresh soot as the ice nucleus. Once the oxidized soot is taken into the water droplet, the ice microscope CCD image becomes dark, so that it is impossible to see the exact placement of the soot. It is unclear whether the soot is well dispersed, but at times it can be seen floating inside the droplet. This is a possible cause for variability of freezing

temperatures within each experiment. It is a possibility that slight movement inside the droplet causes variation in freezing temperature. As seen through observation of the experiment, when soot is visibly moving around in the droplet, there is more variability in the results.

Variations in freezing temperatures of fresh and oxidized soot are most easily observed through inspection of figures involving the full datasets. Each line in the figure is one experimental run showing numerous freezing events. A new particle is used for each experimental run. Figures 17-19 show all freezing events for soot experiments. The data are color coded for fresh versus oxidized soot. Results for 275, 137, and 50 μm diameter soot are shown in Figure 17, 18, and 19, respectively.

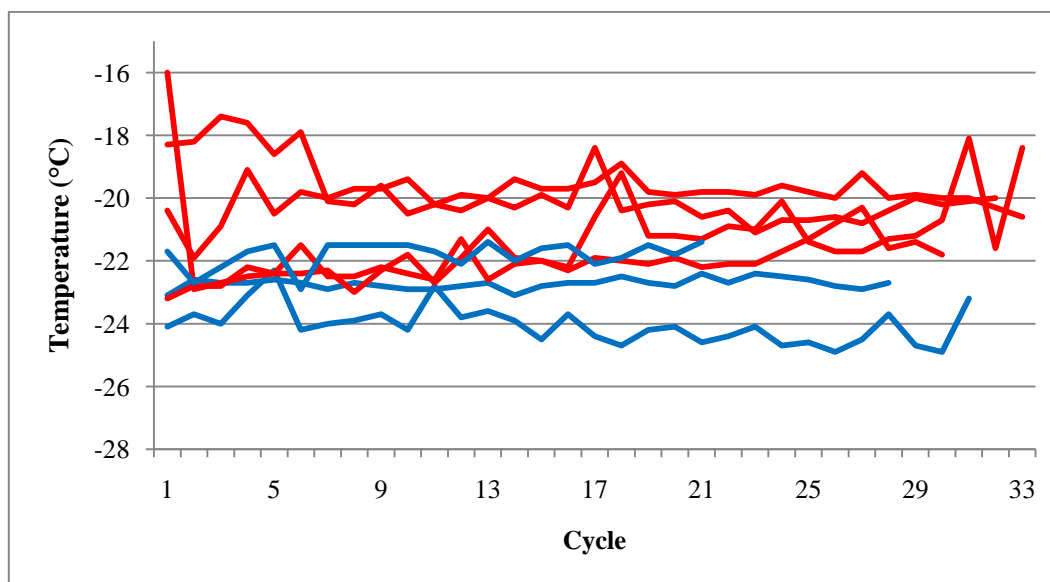


Figure 17. Freezing event temperatures for 275 μm diameter fresh (blue) and oxidized (red) soot particles.

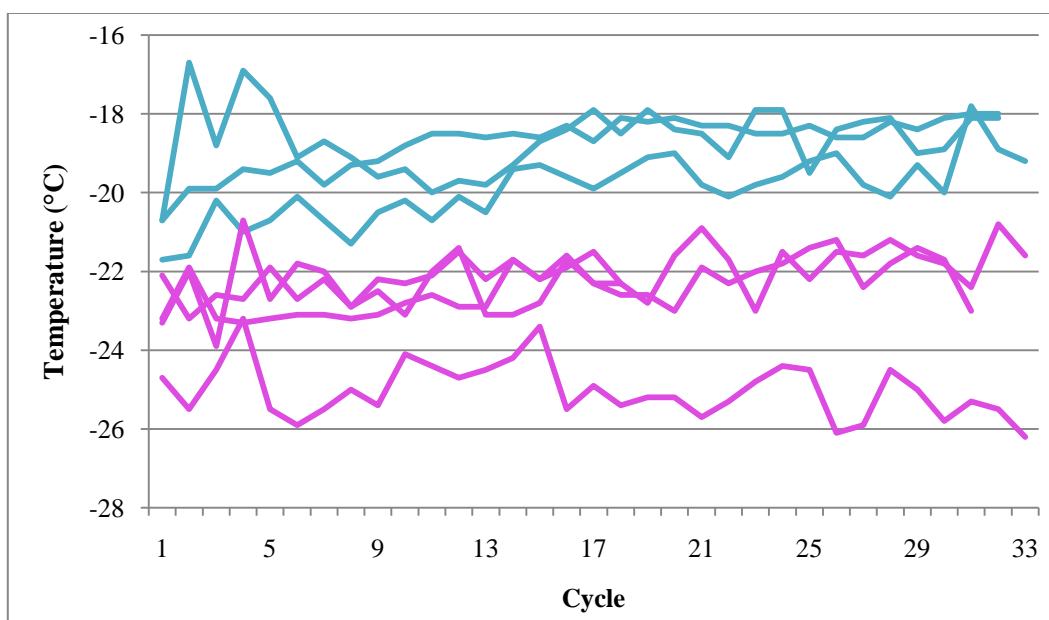


Figure 18. Freezing event temperatures for 137 μm diameter fresh (pink) and oxidized (light blue) soot particles.

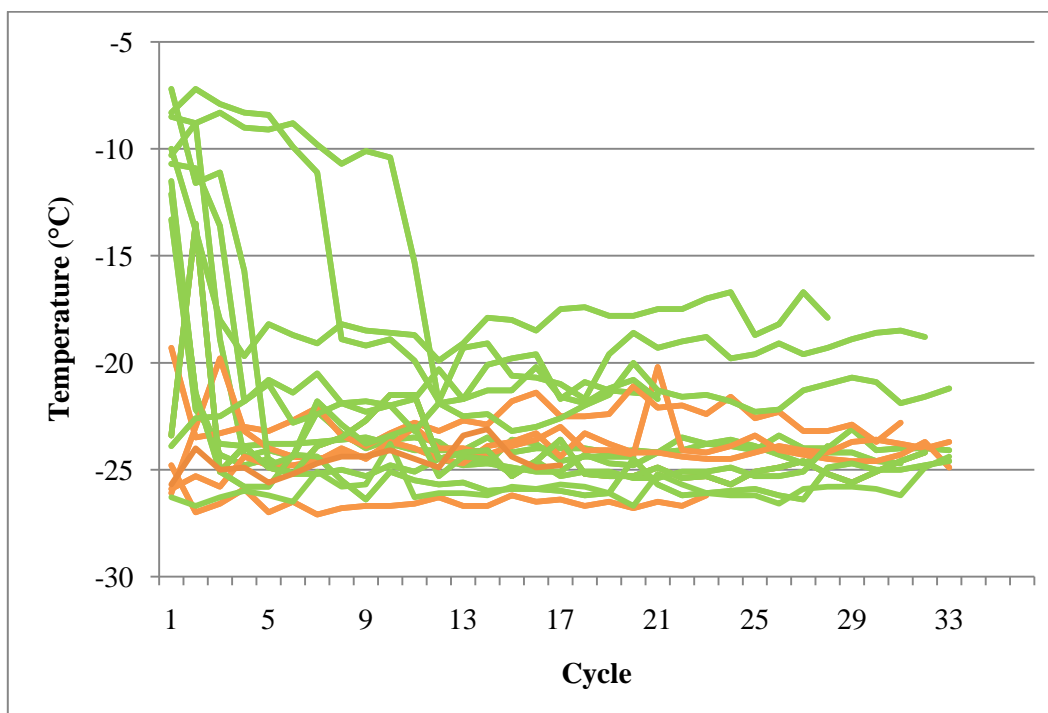


Figure 19. Freezing event temperatures for 50 μm diameter fresh (orange) and oxidized (green) soot particles.

Based on Figures 17 and 18, it appears that oxidized soot are more efficient IN than fresh soot. The average freezing temperatures for fresh and oxidized 275 μm soot are -22.99 $^{\circ}\text{C}$ and -20.73 $^{\circ}\text{C}$, respectively (Table 2). The average temperatures for fresh and oxidized 137 μm soot are -23.05 $^{\circ}\text{C}$ and -19.12 $^{\circ}\text{C}$, respectively. A slight trend is observed in freezing temperature for fresh soot samples (Table 2). The largest size diameter freezes at the warmest temperature, and the smallest size diameter freezes at the coldest temperature. However, this same trend is not seen for oxidized soot. The middle size diameter has the warmest freezing temperature on average. The lack of a trend is most likely due to the highly variable results for the 50 μm soot particles.

In Figure 19 the observations for 50 μm soot show an interesting, yet puzzling result. When the oxidized 50 μm soot is immersed into the water droplet, the freezing for the first few cycles occurs at a very warm temperature. After the first cycles the soot particles seem to lose their efficiency, and freezing events occur at much colder temperatures (near that of fresh soot). This has occurred in 9 out of 11 experiments of oxidized 50 μm soot particles taken from 2 batches of oxidation experiments. It is not clear why this loss of efficiency is occurring for only this size. The oxidized 50 μm soot still freeze at somewhat warmer temperatures on average than fresh soot of the same size.

Table 2. Mean freezing temperatures and pooled standard deviations for fresh and oxidized soot of each size.

Fresh Soot Size (μm)	Mean freezing temp ($^{\circ}\text{C}$)	Pooled Standard Deviation (S_{pooled})	# of Exp	# of Data Points	Oxidized Soot Size (μm)	Mean freezing temp ($^{\circ}\text{C}$)	Pooled Standard Deviation (S_{pooled})	# of Exp	# of Data Points
275	-23.0	1.0	4	117	275	-20.7	1.3	4	99
137	-23.1	1.4	4	122	137	-19.1	1.0	3	97
50	-24.2	1.1	5	163	50	-21.9	4.6	11	314

3.3.1 Soot Statistics

Using the freezing temperatures obtained from ice nucleation experiments for fresh and oxidized soot of average diameter 275, 137, and 50 μm , statistical analysis is performed. From Table 2, the mean freezing temperature and the pooled standard deviation (S_{pooled}) is utilized to carry out a hypothesis test to determine the statistical difference between two average freezing temperatures at the confidence interval of 99%. A pooled standard deviation is more appropriate for this test since the datasets do not have the same number of freezing events for each experiment. S_{pooled} allows each dataset to be weighted individually. The equation for S_{pooled} is:

$$S_{\text{pooled}} = \sqrt{\frac{\sum_{i=1}^N (x_i - \bar{x})^2 + \sum_{j=1}^N (x_j - \bar{x})^2}{N_1 + N_2 - N_s}} \quad (4)$$

The mean freezing temperatures of fresh and oxidized soot of each size are compared to determine if their difference is statistically significantly at a confidence level of 99% using the equation:

$$\bar{x}_1 - \bar{x}_2 = \pm t S_{\text{pooled}} \sqrt{\frac{N_2 - N_1}{N_1 N_2}} \quad (5)$$

where $\bar{x}_1 - \bar{x}_2$ is the difference of the mean between fresh and oxidized of one size or the difference of the mean between two sizes of fresh or oxidized soot. N_1 and N_2 represent the number of observations for each dataset being considered. To find t for each hypothesis test, the degrees of freedom must be determined, where

$$\text{Degrees of freedom} = (N_1 - 1) + (N_2 - 1) \quad (6)$$

The degrees of freedom are input into a t -test table and the appropriate t value for the desired confidence limit is found. Despite degrees of freedom ranging from 200 to 480 depending on the dataset, the average t -value for the 95% confidence limit is 1.97, and the average t -value for the 99% confidence limit is 2.59. Since there was only a difference of ± 0.02 between t -values, the t -value of 2.59 for the 99% confidence limit is used for Equation 5. S_{pooled} of both datasets in consideration is the sum of the individual S_{pooled} values. If the right side of Equation 5 is less than $\bar{x}_1 - \bar{x}_2$, then there is a significant difference in the mean freezing temperature between the two datasets being tested.

Table 3. Statistical data are shown for fresh and oxidized soot of the same size.

	Fresh and Oxidized 275 μm	Fresh and oxidized 137 μm	Fresh and Oxidized 50 μm (all oxidized points)	Fresh and Oxidized 50 μm (1 st oxidized point removed)	Fresh and Oxidized 50 μm (first four oxidized points removed)
Mean (x1-x2)	2.3	3.9	2.3	2.0	1.5
Significant difference	2.3 > 0.4 significant difference	3.9 > 0.4 significant difference	2.3 > 1.0 significant difference	2.0 > 0.9 significant difference	1.5 > 0.8 significant difference

Table 4. Statistical data are shown for fresh soot comparing the different sizes.

	Fresh 275 and 137 μm	Fresh 137 and 50 μm	Fresh 275 and 50 μm
Mean (x1-x2)	0.1	1.1	1.2
Significant difference	0.1 < 0.5 no significant difference	1.1 > 0.5 significant difference	1.2 > 0.4 significant difference

Table 5. Statistical data are shown for oxidized soot comparing different sizes.

	Oxidized 275 and 137 μm	Oxidized 137 and 50 μm	Oxidized 275 and 50 μm (all points)
Mean (x1-x2)	1.6	2.8	1.2
Significant difference	1.6 > 0.6 significant difference	2.8 > 0.8 significant difference	1.2 > 0.7 significant difference

As seen by the tables above, there is a significant difference for all sizes of fresh and oxidized soot. The oxidation of soot warms the temperature at which the sample freezes a significant amount (Table 3). A goal of this research was to explore the influence of the size of the soot particle. Table 4 shows a significant difference for all differing sizes except for fresh soot between the two larger sizes of 275 and 137 μm . Soot with a

diameter of 50 μm showed a strange behavior as seen in the graph illustrating fresh and oxidized 50 μm soot (Figure 19). Judging by the data series in Figure 19, one might assume that the 50 μm particles are initially unsettled until several runs into the experiment. Therefore, statistical analysis is performed not only with all points (Table 3), but with removal of the 1st point (much warmer than the rest) and the first four points (usually warmer). Even with these points removed, there is still a significant difference from fresh to oxidized 50 μm soot.

3.3.2 Discussion of Soot Results

Fresh soot ($-23.4\text{ }^{\circ}\text{C}$) freezes at a cooler temperature than oxidized soot ($-20.6\text{ }^{\circ}\text{C}$) as indicated by the average temperatures for all sizes of soot (Table 2). *Fornea et al.* [2009] shows similar results for fresh soot, which had an average freezing temperature of $-25.6\text{ }^{\circ}\text{C}$. These values for fresh soot agree with another previous study of contact-only freezing of kerosene soot that found freezing temperatures in a range from $-22\text{ }^{\circ}\text{C}$ to $-28\text{ }^{\circ}\text{C}$ [*Diehl and Mitra*, 1998]. These results are important as contact freezing by soot particles is considered one of the most uncertain freezing process [*Hoose et al.*, 2010]. Using oxidized soot as IN is a new topic of research with few studies reporting measured freezing temperatures. Similar results were seen by our research group with an average freezing temperature for oxidized soot of 275 μm diameter of $-22.8\text{ }^{\circ}\text{C}$. When soot is oxidized, functional groups, known as carboxylic acids, are formed on the surface of the soot causing a composition change as seen by FTIR experiments. The warmer freezing temperature for oxidized soot is likely explained by a change in hygroscopicity due to

the oxidation by ozone. The chemical change allows the soot to nucleate by immersion, not contact, freezing and to freeze at a warmer temperature. This result contradicts the results of *Shaw et al.* [2005], which reported colder freezing temperatures by 4-5 °C when IN were immersed in the water droplet. Soot aerosols that activate by both contact and immersion freezing are important to cloud processes in the atmosphere. Our research suggests that unexposed soot aerosols will activate by contact freezing, and exposed soot aerosols will activate by immersion freezing, albeit at warmer temperatures than fresh soot.

A certain amount of variability occurs between ice nucleation experiments using different IN and within one experimental run using the same IN particle. This variability can be attributed to subtle differences from one experiment to the next and differences within the IN itself. Differences in the experiment might include preparation of the droplet and soot particle on the slide which may contribute some, but not all, of the observed variation in freezing temperature. Positioning is important due to the fact that soot does reposition itself during an experiment, possibly causing some variability. Also, intrinsic properties of the soot may cause differences in freezing temperatures.

The oxidized 50 µm soot variability is much higher than the other oxidized and fresh soot experiments. It could be possible that freezing breaks up the soot particles, which is more easily done for those with a smaller diameter. Particle breakup may cause exposure of surface areas on the particle that was not fully oxidized, thus decreasing the availability of active ice nucleation sites on the particle. At the end of the experiment after the humidified flow is turned off, the droplet evaporates. The oxidized soot can be

seen on the microscope slide in the exact location where the droplet was. The oxidized soot pieces have decreased in diameter, which may verify the above hypothesis.

Alternatively, movement of the 50 μm soot particle within the droplet is a possible reason for variability since this soot is the smallest and most mobile within the droplet, as occasionally observed through the microscope images collected during the experiments. Yet another possibility for the variation is that this may be a reversible process in which the oxidized soot is a very efficient ice nucleus, but then reverts to being inefficient. The large variability and interesting behavior of the smallest diameter studied in this research warrants further investigation. Some variability in freezing events is not uncommon, yet there are remaining questions about why it occurs.

Vali [2008] conducted a study on the variability and randomness of IN during immersion freezing. *Vali*'s study also used multiple cycles of freezing and melting like experiments performed in this research. *Vali* [2008] observed changes in freezing temperatures between cycles that in most cases were less than 1 $^{\circ}\text{C}$. However, in one sixth of the cases larger changes were observed, including up to 5 $^{\circ}\text{C}$ variation within one experiment. The conclusion in *Vali*'s study was that the larger changes were due to alterations in IN, including non-random patterns like drifts, jumps, and slow variations. Our experiments have seen similar behavior to those seen in *Vali* [2008]. Similar alterations were seen in about 15% of the author's cycles, leading to a standard deviation of 1.8 $^{\circ}\text{C}$. Other studies found that movement of the nucleus from the interior to the surface led to changes in freezing temperature [*Durant and Shaw, 2005; Shaw et al.,*

2005]. Knowing that fluctuations are common for freezing studies like this one suggests that our data collected are within accurate ranges of temperatures.

3.4 Results of Fresh and Oxidized PAHs as IN

Samples of fresh and oxidized PAHs were used as IN to obtain freezing temperatures. Figures 20, 21, and 22 show the results of ice nucleation experiments for fresh and oxidized samples of anthracene, phenanthrene, and pyrene, respectively.

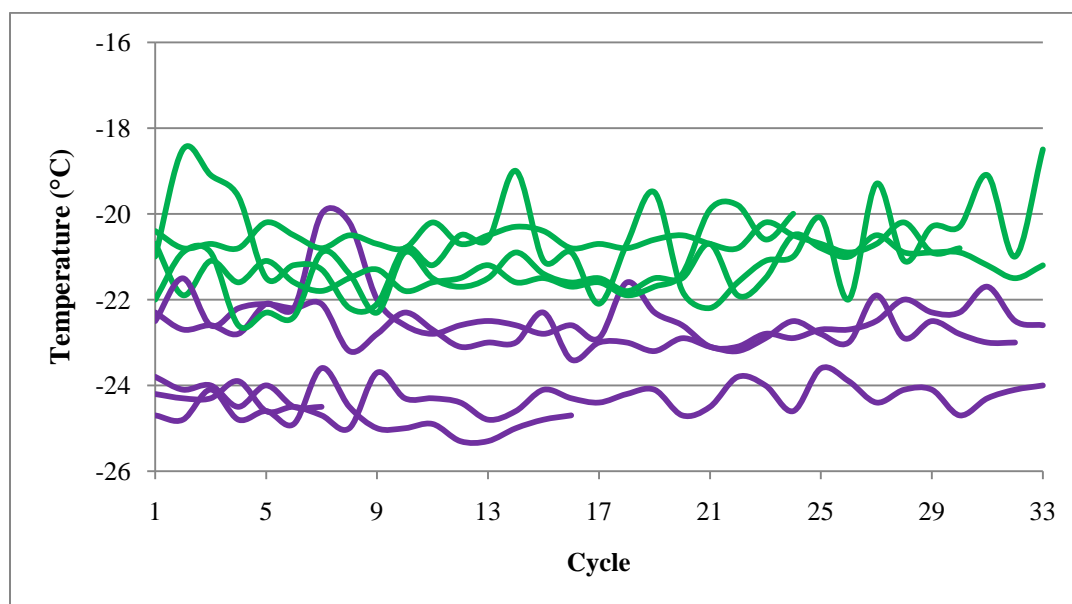


Figure 20. Freezing event temperatures of fresh (purple) and oxidized (green) anthracene particles.

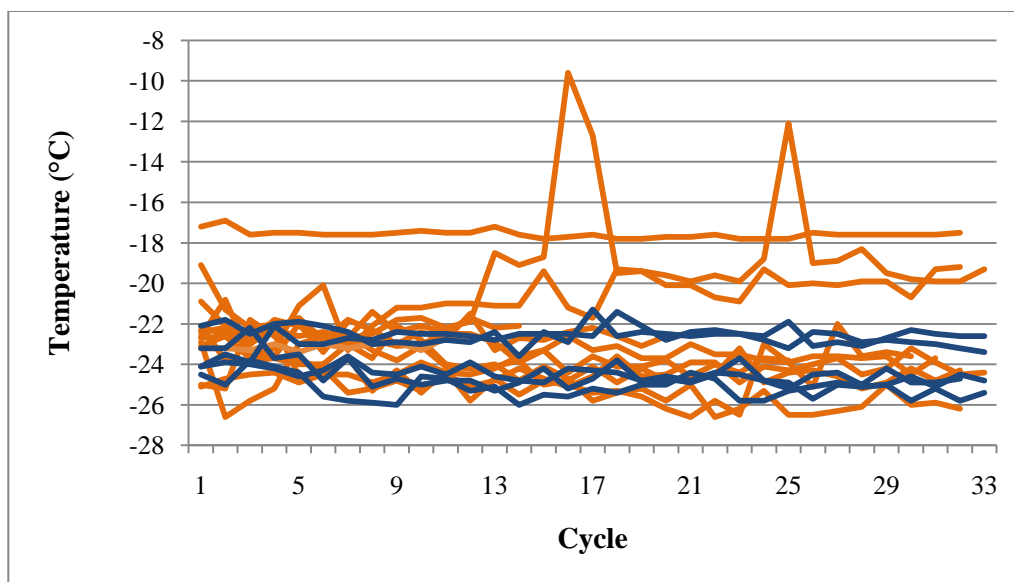


Figure 21. Freezing event temperatures of fresh (navy) and oxidized (orange) phenanthrene particles.

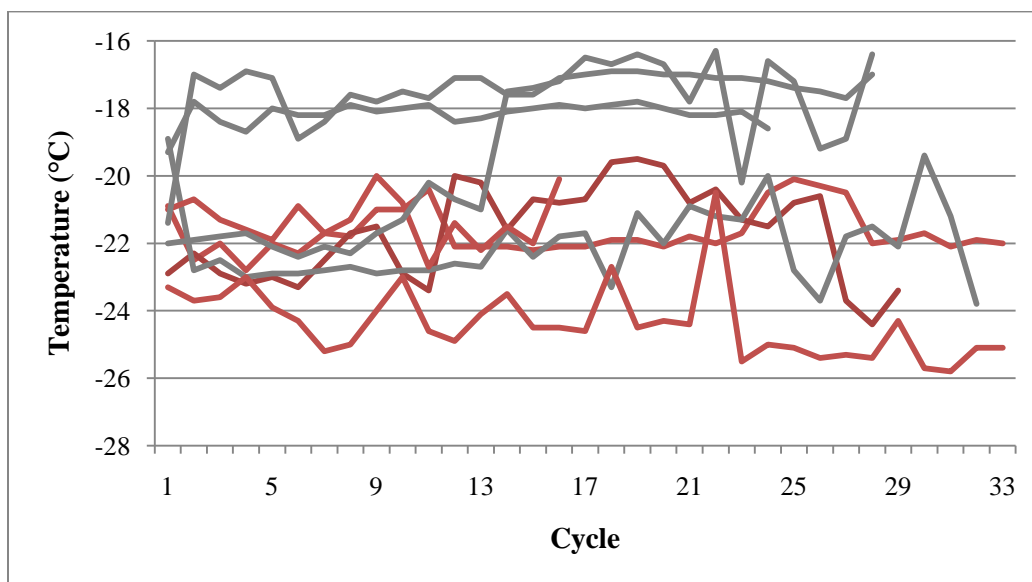


Figure 22. Freezing event temperatures of fresh (red) and oxidized (gray) pyrene particles.

It appears that oxidized PAHs are more efficient IN than fresh PAHs based on Figures 20-22. The average freezing temperatures for fresh and oxidized anthracene are $-23.7\text{ }^{\circ}\text{C}$ and $-20.9\text{ }^{\circ}\text{C}$, respectively (Table 6). The average temperatures for fresh and oxidized phenanthrene are $-23.9\text{ }^{\circ}\text{C}$ and $-22.4\text{ }^{\circ}\text{C}$, respectively. The average temperatures for fresh and oxidized pyrene are $-22.3\text{ }^{\circ}\text{C}$ and $-19.3\text{ }^{\circ}\text{C}$, respectively. Each PAH displayed unique behavior in regards to its position on the water droplet. Table 7 summarizes the observed freezing mechanisms for all IN of all compositions in this research. Note that while the experimental strategy was to initialize each experiment by placing a particle at the surface of the droplet for a contact freezing experiment. However, some particles resisted placement at the droplet surface, and became immersed within in the droplet. Hence, we consider these to be immersion freezing experiments, as further discussed in the following section.

Table 6. Mean freezing temperatures and pooled standard deviations for fresh and oxidized anthracene (anth), phenanthrene (phen), and pyrene.

PAH (fresh)	Mean freezing temp ($^{\circ}\text{C}$)	S_{pooled}	# of Exp	# of Data Points	PAH (oxidized)	Mean freezing temp ($^{\circ}\text{C}$)	S_{pooled}	# of Exp	# of Data Points
anth	-23.7	1.1	5	121	anth	-20.9	0.8	5	136
phen	-23.9	1.2	5	164	phen	-22.4	2.4	13	344
pyrene	-21.3	1.7	4	111	pyrene	-19.3	2.1	4	112

Table 7. The freezing mechanisms for each IN of this study.

Fresh IN	Freezing Mechanism	Oxidized IN	Freezing Mechanism
Soot	Contact	Soot	Immersion
Anthracene	Contact	Anthracene	Contact
Phenanthrene	Contact	Phenanthrene	Immersion/Contact
Pyrene	Contact	Pyrene	Immersion

3.4.1 PAH Statistics

Using Equations 4 and 5, the statistical significance of freezing temperatures for the three PAHs in fresh and oxidized form was found. Fresh and oxidized PAH freezing temperatures were compared using the hypothesis test used in Section 3.3.1 to see if there was a significant difference. The same t-value at 99% confidence level that was previously discussed was inputted into Equation 5. Another hypothesis test was completed to determine whether the ice nucleation activity of PAHs as a whole could be considered or whether the IN ability of individual compounds must be considered separately. In additions, the IN ability of PAHs as a group was compared to that of soot. Tables 8a and 8b reveal the results of the statistical testing using PAH data.

Table 8a. Statistical data are shown for fresh and oxidized PAHs.

	Fresh and Oxidized Anthracene	Fresh and Oxidized Phenanthrene	Fresh and Oxidized Pyrene
Mean (x1-x2)	2.8	1.5	2.0
Significant difference	2.8 > 0.3 significant difference	1.5 > 0.5 significant difference	2.0 > 0.7 significant difference

Table 8b. Statistical data are shown to compare each fresh PAH and each oxidized PAH.

	Fresh Anth and Phen	Fresh Anth and Pyrene	Fresh Phen and Pyrene	Oxidized Anth and Phen	Oxidized Anth and Pyrene	Oxidized Phen and Pyrene
Mean (x1-x2)	0.2	2.4	2.6	1.5	1.6	2.9
Significant difference	0.2 < 0.4 no significant difference	2.4 > 0.5 significant difference	2.6 > 0.5 significant difference	1.5 > 0.6 significant difference	1.6 > 0.5 significant difference	2.9 > 0.7 significant difference

Freezing temperatures for fresh and oxidized anthracene are significantly different from each other. Oxidized phenanthrene shows a large amount of variability between experiments, but the overall temperature difference between fresh and oxidized samples of phenanthrene is still significant. The possible causes of this observed variability for phenanthrene are discussed further in Section 3.4.2. Fresh and oxidized pyrene freezing temperatures differ significantly. When comparing each PAH in fresh or oxidized form, there is no difference between fresh anthracene and fresh pyrene. There was a significant difference between all other PAHs in fresh and oxidized form. Therefore, it is not appropriate to consider the PAHs as one group of IN, but rather each PAH is considered

as individual IN. In all cases, oxidation improves the freezing ability of PAHs, allowing them to facilitate freezing at warmer temperatures than the fresh samples.

3.4.2 Discussion of PAHs as IN

This study has provided freezing temperatures for fresh and oxidized samples of three PAHs: anthracene, phenanthrene, and pyrene. Oxidized PAHs froze at significantly warmer temperatures than fresh PAHs. Each PAH exhibited unique behavior. To understand the freezing events observed, we now report physical observations regarding interactions between the IN and droplets in each case, which may have influenced the observed freezing temperatures. Each PAH acted in a unique way upon introduction to the water droplet and throughout the experiment (Table 7).

When fresh or oxidized anthracene particles were introduced to the water droplet, the IN remained touching the surface of the droplet, yet were inside the droplet. According to *Shaw et al.* [2005], contact freezing can be facilitated equally by a particle adjacent to a droplet surface from the inside or outside. In either configuration, the presence of the IN disrupted the energy of the gas-liquid interface and reduced the energy barrier, which must be overcome in order for the droplet to freeze. There was minimal movement seen after the fresh or oxidized particle made contact with the water droplet. Since the IN particle remained in contact with the water droplet surface throughout the experiment, it is appropriate to assume that anthracene froze by the contact freezing mechanism. Anthracene samples that had been oxidized froze about three degrees warmer than fresh samples. Thus we can conclude that the average freezing temperature for oxidized

anthracene was warmer due to a chemical change. This was caused by the addition of a carboxylic acid, seen by the FTIR, on the surface of the anthracene, which made the IN more wettable.

As evidence by the FTIR spectra, the same chemical change occurred for oxidized pyrene. However, oxidized pyrene immersed into the water droplet upon introduction of the particle to the side of the droplet. There was some variability in freezing temperature for oxidized pyrene. The closer the IN particle was to the middle of the water droplet, the more variable the temperature. Experiments where the oxidized pyrene particle was immersed, yet closer to the surface rather than the middle of the droplet, resulted in less variation and warmer freezing temperatures. Unexposed pyrene remained in contact with the droplet's surface, yet inside the water droplet, for the duration of each experiment.

Fresh phenanthrene also remained in contact with the surface of the water droplet during each experimental run. Figure 21 and Table 6 illustrate the large variability that occurred in oxidized phenanthrene freezing experiments. Although anthracene has a similar structure to phenanthrene, anthracene produced much more constrained results. Much investigation was done to discover why differences occurred between the 13 experiments and within each experiment. A few plausible options became apparent as to why this behavior occurred. The first is simply the intrinsic properties of the IN itself. Each particle selected acts slightly differently adding to the randomness of each freezing experiment. A physical change in the particle during the ice nucleation experiment may cause a change in temperature. During one experiment involving oxidized phenanthrene as the ice nucleus, the particle immersed inside the water droplet was observed breaking

into smaller pieces, which led to a warmer freezing event. The new sharp edges of the particle led to the droplet freezing at $-9.6\text{ }^{\circ}\text{C}$, changing from its previous freezing event temperature of $-18.7\text{ }^{\circ}\text{C}$. A more oxidized area of the particle may have been exposed, leading to a warmer freezing temperature. After the particle broke causing the warm temperature freezing event, the particle stabilized and a cooler freezing temperature resumed. Incomplete oxidation of phenanthrene particles may explain some of the variability. Our standard 24 hour oxidation process allowed a steady ozone concentration of 80 ppm assuming ± 5 ppm to flow over the sample. For oxidized phenanthrene, the oxidation began at 80 ppm then decreased during a portion of the experiment, leading to an average concentration of 63 ppm over the 24 hour oxidation process. This is still a high enough concentration for ozone to react with the PAH molecules, yet the oxidation may have not reached completion. The area under the C=O peak from FTIR measurements was smaller than the other PAHs, which also suggests that the phenanthrene particles were not completely oxidized. Also, previous literature states that phenanthrene may take up to a day to be fully oxidized by ozone in the atmosphere, which is longer than anthracene [Perraudin *et al.*, 2007b]. This property may have impacted the IN experiments.

Another possible reason for variability is a change in position of the IN particle within the water droplet, which causes a change in freezing mechanism during an experiment. Through observation of the experiment, migration of the IN particle from the surface of the droplet toward the center of the droplet was seen. This led to a change from contact freezing to immersion freezing. According to past studies, freezing

temperatures increase by 4-5 °C due to a change from contact to immersion freezing [Durant and Shaw, 2005; Fornea et al., 2009; Shaw et al., 2005]. However, a clear trend in freezing temperature was not found in our experiments perhaps due in part to the changes in mechanisms in some of the experiments. Experiments where the oxidized phenanthrene began at the surface and migrated toward the center of the droplet did not always exhibit the same behavior. Not all experiments where a change in freezing mechanism occurred displayed a wide range of freezing temperatures. Other experiments where the IN was steady in position showed increased variability in freezing temperature. Regardless of what caused the variability for oxidized phenanthrene experiments, the freezing temperatures for oxidized and fresh phenanthrene are significantly different at the 99% confidence level.

3.5 BET Results

We conclude that fresh and oxidized soot have significantly different freezing temperatures and that chemical changes occur at the surface due to oxidation. In addition, physical effects may have occurred as a result of ozone oxidation. Due to the porous nature of soot, using the BET method to calculate the surface area rather than using geometric surface area is more accurate. BET measurements were conducted on sieved samples of fresh and oxidized soot for each size range. Our results are shown in Tables 9 and 10. These results show that surface area calculated by using the BET method does not depend on size. The average specific surface area for fresh and oxidized lampblack soot for all sizes is $21.7 \pm 2.2 \text{ m}^2/\text{g}$ and $21.2 \pm 1.8 \text{ m}^2/\text{g}$, respectively.

Therefore, this is taken to be very accurate data with relative error less than 10%. The BET data agree with *Popovicheva et al.* [2008a], which found the BET surface area of Lampblack carbon to be $22 \text{ m}^2/\text{g}$ [Popovicheva et al., 2008a]. No significant difference in specific surface area is present between fresh and oxidized soot. Similarly, *Aubin and Abbatt* [2003] reported no increase in uptake of nitric acid after soot had been exposed to ozone. Table 9 shows the specific and geometric surface areas for fresh soot samples, while Table 10 shows the same for oxidized soot samples.

Table 9. BET surface area based on mass for fresh soot.

Fresh soot	Run 1		Run 2		Avg BET surface area (m^2/g)	Geometric Surface area	Geometric Surface area	Average Geometric SA
Diameter (μm)	Mass (mg)	BET (m^2/g)	Mass (mg)	BET (m^2/g)		$4*\pi*r^2/\text{mass}$ (m^2/g) for Run 1	$4*\pi*r^2/\text{mass}$ (m^2/g) for Run 2	(m^2/g)
275	53	19.5	47	21.8	20.7	4.48E-06	5.05E-06	4.77E-06
137	33	21.6	46	22.2	21.9	1.79E-06	1.28E-06	1.53E-06
50	15	23.9	19	21.9	22.9	5.24E-07	4.13E-07	4.68E-07

Table 10. BET surface area based on mass for oxidized soot.

Oxidized soot	Run 1		BET (m^2/g)	Radius (m)	Mass (g)	Geometric
Diameter (μm)	Mass (mg)	$4*\pi*r^2/\text{mass}$				
275	20	23.0	0.0001375	2.00E-02	1.19E-05	
137	17	19.4	0.0000685	1.70E-02	3.47E-06	
50	17	22.0	0.000025	1.70E-02	4.62E-07	

A comparison can now be made between geometric surface area and BET surface area for calculating single particle nucleation and probability of freezing, which further provides information on how heterogeneous freezing occurs. The surface area measurements obtained from the BET experiments are used to calculate ice nucleation rates similar to those carried out in *Fornea et al.* [2009] and *Shaw et al.* [2005].

3.6 Application of Classical Nucleation Theory

Despite recent research dedicated to studying heterogeneous ice nucleation, scientists have not agreed on a theory. Additionally, it is not known what the dominant freezing mechanism is at temperatures above ~ -40 °C. Classical nucleation theory assumes ice nucleation to be a stochastic process [*Fletcher*, 1962]. Classical nucleation theory, however, was not originally formulated to describe heterogeneous ice nucleation. In order to apply classical nucleation theory to heterogeneous ice nucleation events, a few assumptions must be made. First, the entire surface area of the IN particle is assumed to interact with the water droplet. In addition, differences in contact and immersion freezing mechanisms are ignored. Despite these limitations, classical nucleation theory is an acceptable starting point to explore heterogeneous processes.

An adaptation of classical nucleation theory for heterogeneous ice nucleation was developed by *Fletcher* [1962]. *Fletcher* presented classical nucleation theory equations that continue to be the most tested and widely used in the ice nucleation field. Classical nucleation theory describes single particle heterogeneous nucleation rate by the following equation:

$$J = 4\pi r_N^2 K \exp\left[\frac{\Delta G^*}{k_B T}\right] \quad (7)$$

Here, r_N represents the radius of the IN, K represents the kinetic coefficient, ΔG^* represents the Gibbs free energy of the formation of a critical ice embryo on the surface of the IN, k_B represents the Boltzmann constant, and T represents the temperature in Kelvin [Fletcher, 1962; Fornea et al., 2009; Shaw et al., 2005]. The Gibbs free energy term (ΔG^*) is the most variable and dominant value for this equation and for the modified form of single-particle nucleation rate for supercooled water [Fletcher, 1962], which is:

$$J \approx \frac{k_B T}{h} 4\pi r_N^2 n'_c \exp\left[-\frac{\Delta g}{RT} - \frac{\Delta G^*}{k_B T}\right] \quad (8)$$

This corrected equation for single-particle nucleation rate takes into account activation energy of water molecules diffusing across the solid-liquid interface (Δg). The additional exponential term also includes an expanded kinetic coefficient that contains Planck's constant (h) the number of water molecules in contact with a unit area of the IN surface area (n'_c) [Fletcher, 1969; Fornea et al., 2009]. The Gibbs free energy term is the most dominant variable in the exponential term and is defined as:

$$\Delta G^* = \frac{16\pi M_w^2 \sigma_{i/w}^3 f(m_{i/w}, x)}{3k_B T (n_i l_f)^2 \Delta T^2} \quad (9)$$

In this equation, M_w represents the molecular weight of water, $\sigma_{i/w}$ represents the interfacial free energy per unit area between ice and liquid water (surface tension), f represents the wetting parameter, n_i represents the number of molecules per unit volume for ice, l_f is the latent heat of fusion for water, and ΔT is the difference between the melting point of water and the given temperature [Fletcher, 1962; 1969; Fornea et al., 2009; Shaw et al., 2005]. Note that the f term in the above equation is the only variable that changes based on size and composition of the IN. As seen above, f is a function of the contact parameter, $m_{i/w}$, which is equal to the cosine of the contact angle, θ , between the ice embryo and the ice nucleus.

$$m_{i/w} = \cos \theta \quad (10)$$

The f term also varies with χ , which is the ratio of IN radius to critical radius of ice embryo [Fornea et al., 2009].

3.6.1 Probability of Freezing

Probability is conventionally used to explain ice nucleation because, according to classical nucleation theory, freezing is a stochastic process. Probability is related to nucleation rate through the following equation:

$$P \equiv \frac{N_f}{N_0} = 1 - \exp\left(-\int_0^t J dt\right) \quad (11)$$

In this equation, N_0 is defined as the total number of droplets, N_f is defined as the number of those droplets that have frozen at a certain temperature, J is the single particle

heterogeneous nucleation rate, and t is the time elapsed over an experiment [Fornea *et al.*, 2009; Shaw *et al.*, 2005]. By inputting J from Equation 8 into Equation 11, theoretical probability curves with parameters similar to those IN used in ice nucleation experiments were calculated. The theoretical curves represent the probability (y-axis) that a water droplet will have frozen at a given temperature (x axis) [Fornea *et al.*, 2009].

Since a large number of freezing temperatures were obtained from the experiments performed in this study, an ‘empirical’ probability of freezing as a function of temperature can be produced [Shaw *et al.*, 2005]. All the freezing temperatures for each composition are combined to produce empirical probability curves (Figures 23a-d). The empirical probability curves of fresh and oxidized soot and PAHs clearly indicate that there is a higher likelihood of freezing for oxidized IN compared to fresh IN. Figures 23a-d illustrate how the likelihood of freezing is dependent upon composition. The information on nucleation efficiency obtained from the probability curves is limited in its usefulness by the classical nucleation theory. Note that all other variables remain constant, and the probability curves calculated from the classical nucleation theory are merely translated right or left depending on the f value while remaining identical in shape. Therefore, more parameters are needed to improve the uncertainty in any conclusions made about ice nucleation efficiency.

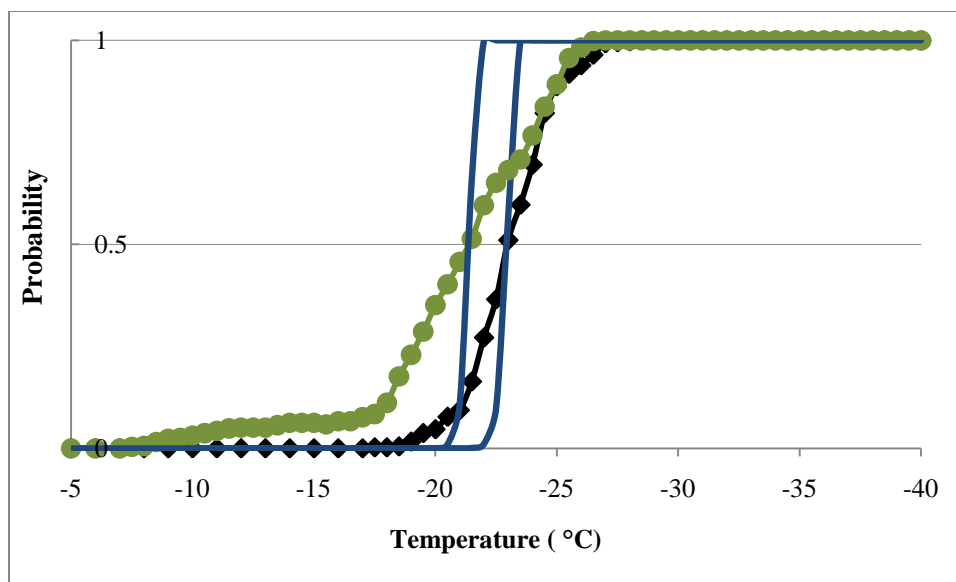


Figure 23a. Empirical probability curves for fresh (black) and oxidized (green) soot and theoretical probability curves for fresh and oxidized soot (blue).

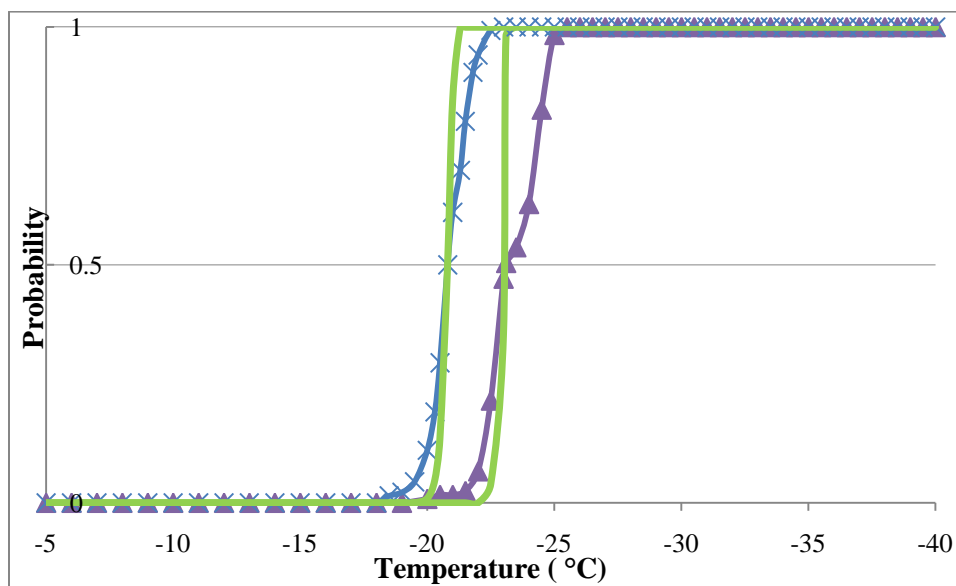


Figure 23b. Empirical probability curves for fresh (purple triangles) and oxidized (blue x) anthracene and theoretical probability curves for fresh and oxidized anthracene (green line).

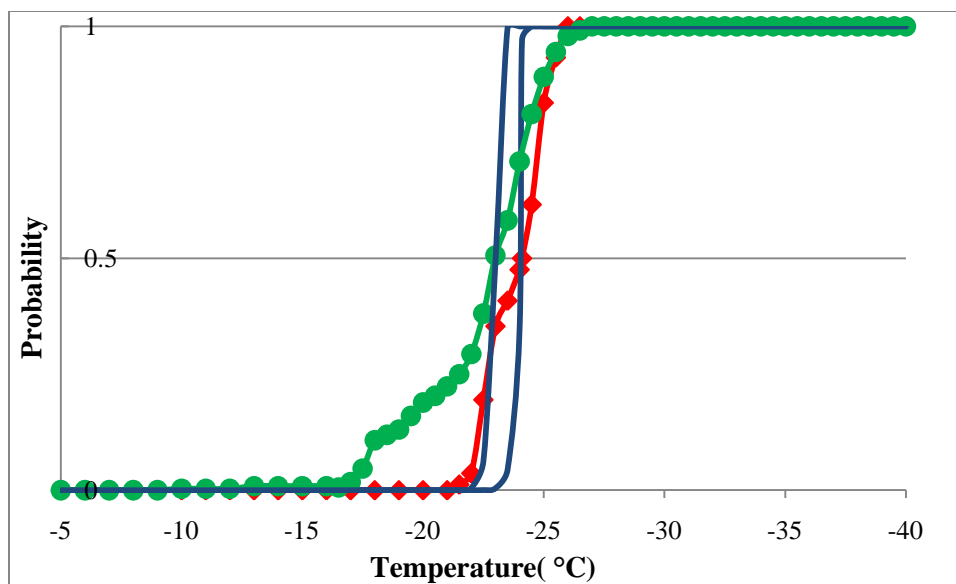


Figure 23c. Empirical probability curves for fresh (red diamonds) and oxidized (green circles) phenanthrene and theoretical probability curves for fresh and oxidized (navy line) phenanthrene.

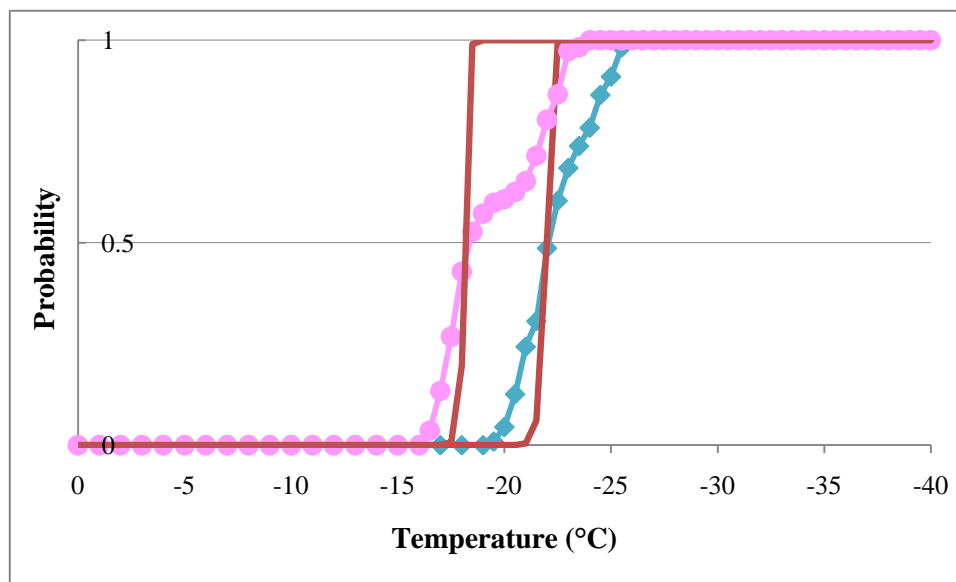


Figure 23d. Empirical probability curves for fresh (aqua diamonds) and oxidized (pink circles) pyrene and theoretical probability curves for fresh and oxidized (red line) pyrene.

The theoretical probability curves were fitted to the empirical probability curves at 50% probability levels in order to obtain a best fit value for the wetting parameter (f). The f value varied based on composition and freezing mechanism [Shaw *et al.*, 2005]. The best fit f value was 0.400 for fresh soot and 0.346 for oxidized soot (Table 11). This corresponds to freezing temperatures of -23.0 °C and -21.4 °C, respectively. The best fit f values for fresh and oxidized PAHs are found in Table 11.

Table 11. Calculated wetting parameter, f , for all IN sizes and compositions in this study are reported. This f value was obtained by taking the empirical probability for each size, then inputting geometric surface area using average radius for each size to find the f value at 50% probability.

IN Size and Composition	Wetting parameter (f)	IN Composition (all 137 μm diameter)	Wetting parameter (f)
All Sizes Fresh Soot	0.400	Fresh Anthracene	0.447
Fresh 275 μm Soot	0.398	Fresh Phenanthrene	0.489
Fresh 137 μm Soot	0.384	Fresh Pyrene	0.403
Fresh 50 μm Soot	0.419		
All Sizes Oxidized Soot	0.346	Oxidized Anthracene	0.359
Oxidized 275 μm Soot	0.350	Oxidized Phenanthrene	0.443
Oxidized 137 μm Soot	0.271	Oxidized Pyrene	0.287
Oxidized 50 μm Soot	0.394		

The f values for each size are near that of the overall best fit f for fresh or oxidized soot. The f value varied from 0.384 to 0.419 for fresh soot with the f value for all sizes being 0.400. The f value varied from 0.271 to 0.394 for each size of oxidized soot with the overall f for oxidized soot being 0.346. The variation between the wetting parameter for fresh and oxidized soot implies that a change in composition and freezing mechanism has occurred. The wetting parameter, f , provides information regarding the efficiency of

ice nucleation for each IN composition. An ice nucleus with a higher contact angle has a higher wetting parameter f , and a higher f translates to a smaller nucleation rate, meaning the ice nucleus is less efficient. Our results show that oxidized soot is a more efficient ice nucleus based on the f value, higher likelihood of freezing, and warmer freezing temperatures.

The wetting parameters were also used to calculate nucleation rates and compare ice nucleation efficiency of soot particles based on the size of the soot particle. Using the dataset for each size of fresh and oxidized soot, f values were obtained and are given in Table 11. Figure 24 illustrates the empirical probability curves for each size of fresh and oxidized soot. The curves were matched at 50% probability with the theoretical curve to obtain the f value as above. The curves given in Figures 23a and 24 and the results in Table 11 show that f is lower for oxidized soot and implies that it is a more efficient IN than fresh soot. Results for fresh soot follow a slight size trend with the largest size being the most efficient, as one would expect. However, the probability curves for the two larger sizes overlap (Figure 24). In contrast, the oxidized results do not follow the expected size trend, which may be caused by complications resulting from the oxidation process. The middle size (137 μm) diameter of oxidized soot is the most efficient IN based on f and ice nucleation temperature data. Furthermore, the smallest size soot particle is most efficient in the first few cycles of the experiment, and then reverts to being as efficient as the smallest size of fresh soot. Theory suggests that larger size would provide more surface area, and the ice nucleus would promote freezing at warmer temperatures. The range of 300 to 50 μm diameter may be too small to see a definite size

effect, or other factors may play a role in temperatures of freezing events observed here. Our results agree with past findings that state if the size of the IN is changed, meaning the χ variable changes, there is very little effect on the magnitude of f for IN in this size range [Fornea et al., 2009]. This may explain why size does not seem to influence nucleation efficiency based on small changes in f value. Therefore, according to our results, the size of the soot particle does not have a direct relationship to ice nucleation efficiency.

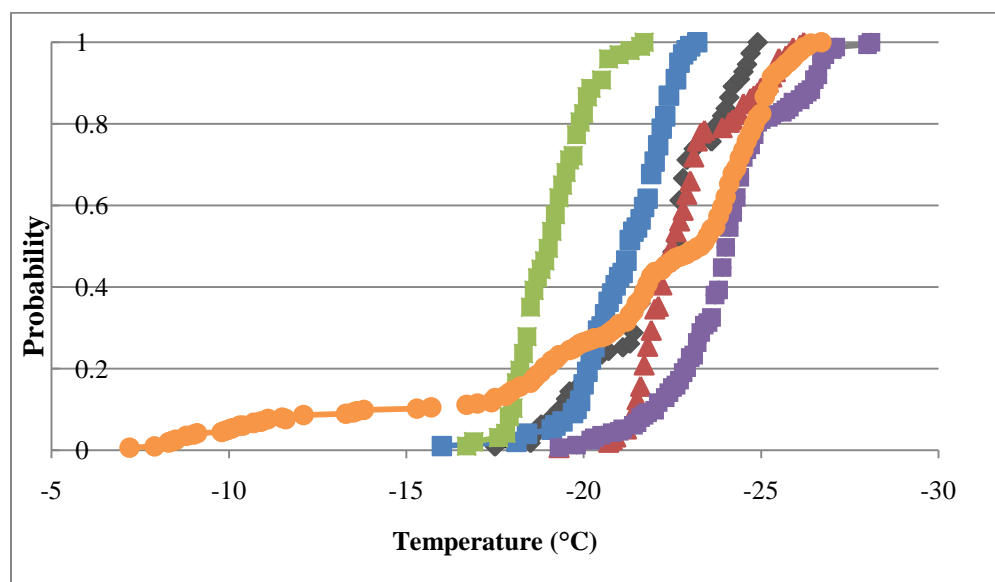


Figure 24. The empirical probability curves for each size of fresh and oxidized soot are shown: fresh 275 μm (black), oxidized 275 μm (blue), fresh 137 μm (red), oxidized 137 μm (green), fresh 50 μm (purple), and oxidized 50 μm (orange).

Next we compare results for each of the PAHs. Table 11 shows that the oxidized PAHs have smaller wetting parameters than the fresh PAHs. Also Figure 23b-d show that freezing temperatures for oxidized PAHs are higher. This further confirms that the

oxidation process causes a change in efficiency and freezing temperature for the PAHs in this study. The variability in freezing temperature that occurred for some experiments can also be seen by the empirical probability curves. The more horizontal the probability curve, the more variability occurred in freezing temperatures. A more upright empirical probability curve indicates there is less variability in freezing temperature for the IN composition. For example, the oxidized anthracene empirical probability curve (Figure 23b) has the most vertical shape and matches the theoretical probability curves that follow the stochastic theory very well. This dataset had the smallest standard deviation due to a smaller amount of variability in freezing temperature. However, in other cases, such as the phenanthrene experiments, the fit to classical nucleation theory is correct in form, but not well constrained. In Section 3.6.3 below, we look to a new model in an attempt to explain freezing in instances where the fit to classical nucleation theory needs improvement [Niedermeier *et al.*, 2011]. This mixed stochastic-singular model bridges the two competing theories on ice nucleation to create a more flexible model which we use here to explore our empirical probability curves.

3.6.2 Heterogeneous Nucleation Rates for Soot and PAHs

Homogeneous nucleation rates are consistent between different experimental studies [Pruppacher and Klett, 1997]. Heterogeneous nucleation rates, however, depend on the freezing mechanism, IN composition and size, temperature, and other variables. These dependencies cause heterogeneous nucleation rates to vary greatly [Demott, 1995; Kanji and Abbatt, 2006; Kanji *et al.*, 2008]. Despite the assumptions and uncertainties in

classical nucleation theory, it is advantageous to report the heterogeneous nucleation rates associated with this research. This study contributes to the growing amount of research that reports mechanism-specific nucleation rates. This information is important since heterogeneous nucleation rates help to describe freezing in the atmosphere and to determine which mechanism is dominant under atmospheric conditions [Hoose *et al.*, 2010]. Heterogeneous nucleation rates can be applied in global climate models to estimate how much influence ice nucleation has in the atmosphere. One global simulation model that used classical nucleation theory estimated that 23% of IN that initiate ice nucleation are carbonaceous aerosols [Hoose *et al.*, 2010]. A larger database of heterogeneous nucleation rates is needed to improve modeling studies. The heterogeneous nucleation rates calculated in this research can be compared to the data already available by using a normalized form of the nucleation rate, J .

Equation 8 was used to derive a single particle nucleation rate, which gives rate in the unit of event per time per particle in s^{-1} , scaled by the surface area of the ice nucleus. A normalized form of this equation is obtained if the $4\pi r_N^2$ is removed, yielding a heterogeneous nucleation rate equation with units per area per time per particle, in $cm^{-2} s^{-1}$. By using this variation of the heterogeneous nucleation equation, a rate is found for each experimental group at a specific temperature, which allows a comparison of the relative nucleation efficiency for each group at a given temperature (Figure 25a). The heterogeneous nucleation rate is reported at the temperatures of 0 °C, -15 °C, -20 °C, -25 °C and -30 °C for each group. The best fit value of f for each group was used in the

calculation of the nucleation rate to estimate the fraction of an ambient population of particles frozen at a given temperature.

Figure 25a shows the normalized nucleation rate for each IN composition at a specific temperature. IN composition and freezing temperature play vital roles in the nucleation efficiency. Higher nucleation rates indicate that the specific IN is more likely to nucleate than an IN with a lower nucleation rate. The results from Figure 25a show that oxidation improves the nucleation efficiency for all IN types. The results from f values and probability calculations also show an increase in efficiency and probability of freezing when the aerosol is oxidized. Figure 25b uses the same idea as Figure 25a, but uses the percentage of droplets that had frozen in a one minute time period at the same specific temperatures based on our freezing temperature data. This juxtaposition helps to link a calculated nucleation rate with estimates of the fraction of various types of aerosols frozen in the ambient atmosphere. With the exception of oxidized soot, all IN had less than 1 % of droplets nucleated at -15 °C. 100% were frozen by -30 °C, while over 80% of droplets had frozen by -25 °C. The drastic change that occurs for most IN between -20 °C and -25 °C shows that this is the temperature range where most nucleation occurs. Droplets exposed to temperatures warmer than -20°C rarely freeze. Figures 25a and Figure 25b help to quantify freezing efficiency based on equations from classical nucleation theory. In order of least efficient to most efficient: fresh phenanthrene, fresh anthracene, fresh soot, oxidized phenanthrene, fresh pyrene, oxidized anthracene, oxidized soot, and oxidized pyrene.

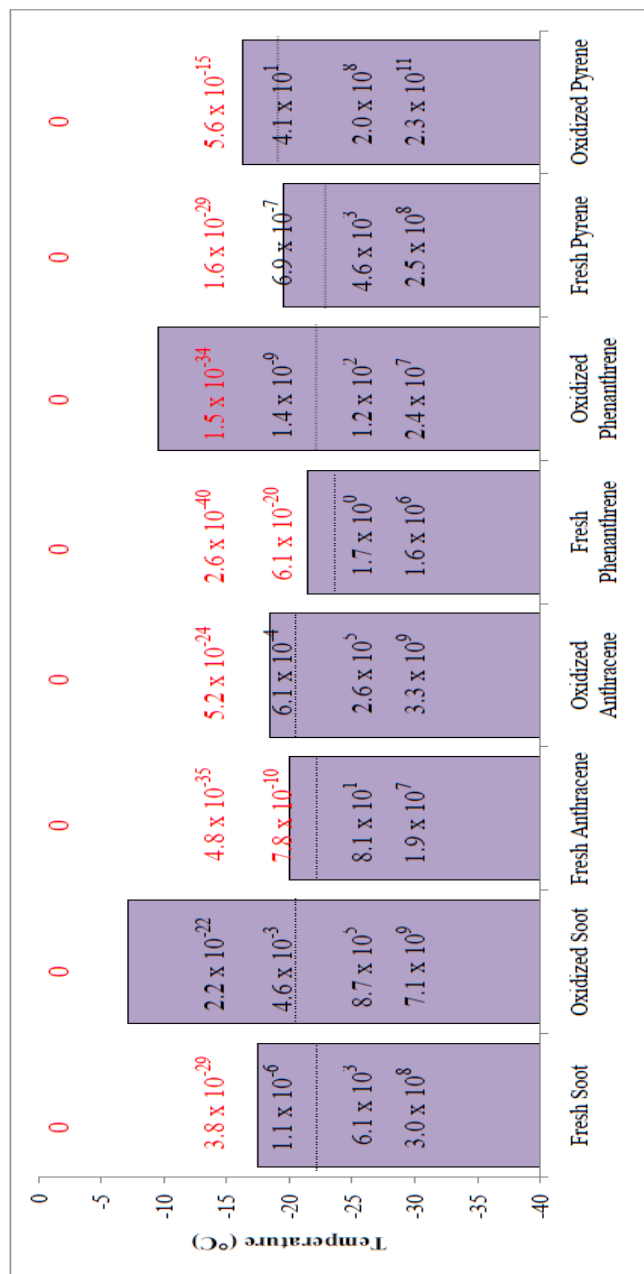


Figure 25a. Calculated normalized heterogeneous nucleation rates ($\text{cm}^2\text{sec}^{-1}$) using best fit of f are shown. Purple regions represent temperature range that fresh and oxidized IN would activate based on experimental data. Rates of 0 indicate no ice nucleation occurred in that range for our experimental data. The horizontal dotted line located within the purple regions indicates the temperature at which 50% of our freezing events had occurred.

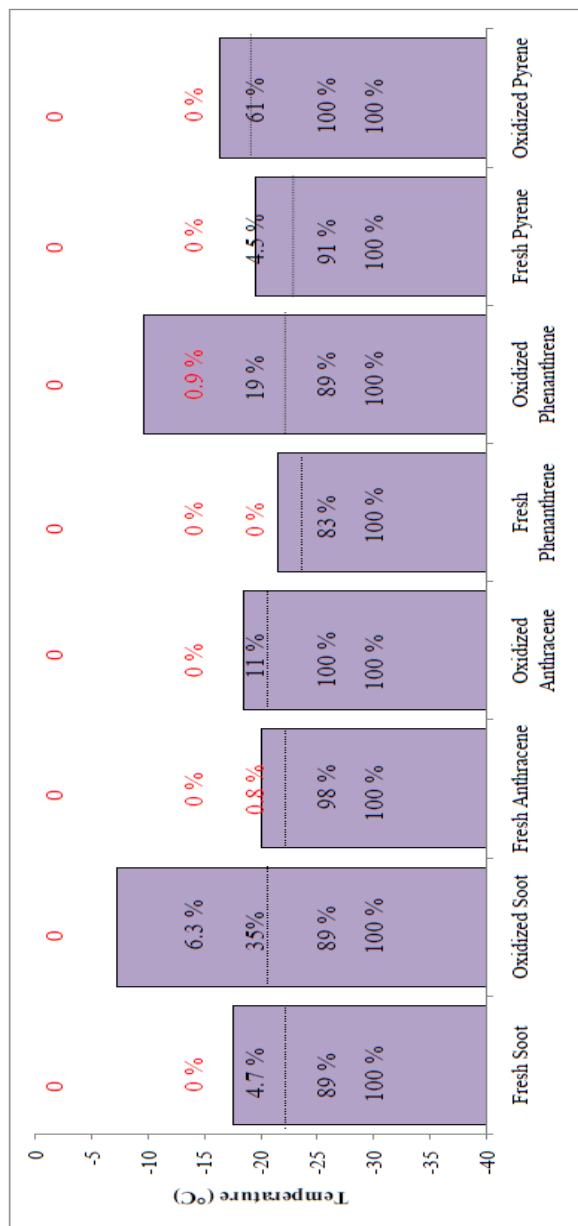


Figure 25b. The percentage of droplets containing a specific IN that have nucleated in one minute at a specific temperature is reported. The percentages are taken from data used to make the empirical probability curves.

Table 12. Heterogeneous nucleation rates, J (single particle) and J (normalized), for fresh and oxidized PAHs.

PAHs	J (with SA)(sec ⁻¹)	J (normalized) (cm ⁻² sec ⁻¹)
Fresh Anthracene	-15 °C: 2.8 x 10 ⁻³⁶	-15 C: 4.8 x 10 ⁻³⁵
	-20 °C: 4.6 x 10 ⁻¹¹	-20 C: 7.8 x 10 ⁻¹⁰
	-25 °C :4.8 x 10 ⁰	-25 °C: 8.1 x 10 ¹
	-30 °C: 1.1 x 10 ⁶	-30 C: 1.9 x 10 ⁷
Oxidized Anthracene	-15 °C: 3.1 x 10 ⁻²⁵	-15 °C: 5.2 x 10 ⁻²⁴
	-20 °C: 3.6 x 10 ⁻⁵	-20 °C: 6.1 x 10 ⁻⁴
	-25 °C : 1.6 x 10 ⁴	-25 °C: 2.6 x 10 ⁵
	-30 °C: 2.0 x 10 ⁸	-30 °C: 3.3 x 10 ⁹
Fresh Phenanthrene	-15 °C: 1.5 x 10 ⁻⁴¹	-15 °C: 2.6x 10 ⁻⁴⁰
	-20 °C: 7.0 x 10 ⁻¹⁴	-20 °C: 6.1 x 10 ⁻²⁰
	-25 °C : 1.0 x 10 ¹	-25 °C: 1.7 x 10 ⁰
	-30 °C: 1.8 x 10 ⁵	-30 °C: 1.6 x 10 ⁶
Oxidized Phenanthrene	-15 °C: 9.0 x 10 ⁻³⁶	-15 °C: 1.5 x 10 ⁻³⁴
	-20 °C: 8.5 x 10 ⁻¹¹	-20 °C: 1.4 x 10 ⁻⁹
	-25 °C : 6.9 x 10 ⁰	-25 °C: 1.2 x 10 ²
	-30 °C: 1.4 x 10 ⁶	-30 °C: 2.4 x 10 ⁷
Fresh Pyrene	-15 °C: 9.4 x 10 ⁻³¹	-15 °C: 1.6 x 10 ⁻²⁹
	-20 °C: 4.1 x 10 ⁻⁸	-20 °C: 6.9 x 10 ⁻⁷
	-25 °C : 2.7 x 10 ²	-25 °C : 4.6 x 10 ³
	-30 °C: 1.5 x 10 ⁷	-30 °C: 2.5 x 10 ⁸
Oxidized Pyrene	-15 °C: 3.3 x 10 ⁻¹⁶	-15 °C: 5.6 x 10 ⁻¹⁵
	-20 °C: 2.4 x 10 ⁰	-20 °C: 4.1 x 10 ¹
	-25 °C: 2.4 x 10 ⁷	-25 °C: 2.0 x 10 ⁸
	-30 °C: 1.1 x 10 ¹⁰	-30 °C: 2.3 x 10 ¹¹

The heterogeneous nucleation rates for PAHs can be further compared in Table 12. J (normalized), which is reported in Figure 25a, and J (single particle) can be compared to see how including surface area changes heterogeneous nucleation rates. The information from Tables 11 and 12 shows conclusively that oxidizing PAHs increases the nucleation efficiency. These results show that the least efficient PAH is fresh phenanthrene, and the most efficient PAH is oxidized pyrene.

The effect of the size of the soot particle on nucleation efficiency can be further explored using nucleation rates (Table 13). The three chosen diameters for soot particles are inputted into the surface area term in the single particle J equation along with the best fit f value for each size. The normalized J removes this surface area term but uses the same f value. The two J values are compared in Table 13 at one temperature, where nucleation begins to occur (-20 °C).

Table 13. Different sizes of soot are compared using nucleation rates, J (single particle) and J (normalized).

IN Size and Composition	J (with $4\pi r_N^2$) at -20 °C (s^{-1})	J (normalized) at -20 °C ($cm^{-2}s^{-1}$)
All Sizes Fresh Soot	6.5×10^{-10}	1.1×10^{-6}
Fresh 275 μm Soot	2.9×10^{-9}	1.5×10^{-6}
Fresh 137 μm Soot	7.6×10^{-9}	1.3×10^{-5}
Fresh 50 μm Soot	4.5×10^{-12}	5.8×10^{-6}
All Sizes Oxidized Soot	2.7×10^{-6}	4.6×10^{-3}
Oxidized 275 μm Soot	4.8×10^{-6}	2.5×10^{-3}
Oxidized 137 μm Soot	2.9×10^{-1}	4.8×10^2
Oxidized 50 μm Soot	2.2×10^{-10}	2.8×10^{-6}

One goal of this study was to compare the three sizes of sifted soot to see if there was a trend in nucleation efficiency. While a significant difference is seen for all sizes of fresh soot except between 275 and 137 μm , the overall averages did not show a clear result. Fresh soot results showed that the soot with the largest diameter have the warmest freezing temperatures and the smallest soot have the coldest freezing temperatures, yet

not all are significantly different. However, results for oxidized soot were significantly different between sizes, but the logical trend was not followed with the middle size diameter having the warmest freezing temperature. Figure 24 showed that the size trend was actually reversed for oxidized soot. In addition, BET results do not show a change in surface area between sizes of soot or between fresh and oxidized samples. By comparing J (single particle) for each size of fresh and oxidized soot, the nucleation efficiency between sizes can be explored. There is no clear trend in nucleation rate and subsequently the nucleation efficiency of soot based on size. *Pruppacher and Klett* [1977] state there is stronger size dependence for small sizes. The micron size particles used in this study are very large by atmospheric standards and may be collectively in the bulk regime, which is insensitive to difference due to size. Also, the lack of size dependence could be due to the smaller difference of only a range of 250 μm diameter that a clear effect on IN efficiency is not seen. Previous literature suggests larger sizes are most efficient at nucleating but only when considering smaller sizes (i.e. hundreds of nanometer diameter) with a larger range of sizes [*Pruppacher and Klett, 1997; Seinfeld and Pandis, 2006*]. This study shows no clear trend in nucleation efficiency for a diameter ranging from at most 300 μm to smallest of 48 μm .

3.6.3 Evaluation of Further Constraints on Nucleation Theory

Additional calculations were performed to test whether probability and nucleation rates could be better refined based on our measurements. Surface area measurements obtained using the BET method are considered more accurate than geometric

calculations due to the porous nature of soot particles. The BET surface area for the soot sample was multiplied by density and volume of a single particle so that the BET surface of a single particle could be inputted into the equation for single particle nucleation rate. By inputting the BET surface area into Equation 7, different values for J , f , and probability were found. The probability curves created by inputting BET surface area were very similar to those formed from using geometric surface area. Also, probability curves using each size of soot show there was no difference in probability based on size when using BET or geometric surface area. New f values for fresh and oxidized soot were determined using the altered calculations with the BET surface area, but the temperature values at 50% probability remained the same (Table 14). The change in the wetting parameter was not significant enough to change the probability curve. For fresh and oxidized soot the f values were larger, implying less efficient ice nucleation, than that found using geometric surface area. J (single particle) and J (normalized) were calculated using the new f value and with the adjustment in surface area. The J (single particle) may be more useful since it includes the surface area measurement. J (normalized) does not include surface area, yet differs from previous calculations based on the change in f .

The values for f and J (single particle and normalized) calculated using BET surface area (Table 14) compared to f and J using geometric surface area (Table 10) imply that soot particles are less efficient IN than we would conclude based on geometric surface area. Calculations based upon geometric surface area may overestimate the efficiency of IN such as soot that are porous. J (single particle) and J (normalized) were both

calculated at specific temperatures. J (single particle) and J (normalized) are larger using geometric surface area compared to BET surface area. However, J (normalized) may not be the best parameter to use since the surface area component has been removed.

Table 14. The best fit value of f , J (with surface area) and J (normalized) for oxidized and fresh soot using BET surface area measurements.

IN	f	J (s^{-1})	J (normalized) ($cm^{-2}s^{-1}$)
Fresh Soot (all sizes)	0.616	-15 °C: 5.0×10^{-49}	-15 °C: 3.1×10^{-56}
		-20 °C: 5.9×10^{-14}	-20 °C: 3.7×10^{-21}
		-25 °C: 2.3×10^2	-25 °C: 1.4×10^{-5}
		-30 °C: 1.4×10^{10}	-30 °C: 8.8×10^2
Oxidized Soot (all sizes)	0.528	-15 °C: 5.3×10^{-38}	-15 °C: 3.4×10^{-45}
		-20 °C: 4.6×10^{-8}	-20 °C: 2.9×10^{-15}
		-25 °C: 7.4×10^5	-25 °C: 4.7×10^{-2}
		-30 °C: 2.5×10^{12}	-30 °C: 1.6×10^5

Scientists continue to debate whether heterogeneous ice nucleation is a stochastic process or a singular process. The stochastic theory assumes heterogeneous freezing to be a stochastic process just as homogeneous freezing does [Niedermeier *et al.*, 2011; Pruppacher and Klett, 1997; Shaw *et al.*, 2005; Vali, 2008]. The stochastic theory is time dependent with a droplet containing an ice nucleus having an equal chance of freezing in a given time frame compared to the other droplets in that population. In contrast, the singular hypothesis states that there is a determined temperature at which active sites allow freezing to occur [Langham and Mason, 1958; Niedermeier *et al.*, 2011]. Further, all droplets freeze once the threshold temperature is reached. Lastly, the singular hypothesis is considered time-independent. In reality, it seems that some particles

contain active sites on which preferential ice nucleation occurs due to a minimum in particle-ice interfacial free energy. However, why these sites are preferred is unknown. It may be due to the sites having a geometric shape similar to the ice lattice structure, hydrogen bonds of specific polarity, or sharp edges that could enhance ice nucleation [Niedermeier *et al.*, 2011].

To fully explain observed ice nucleation behavior, a model which combines aspects of both singular and stochastic behavior has recently been proposed by Niedermeier *et al.* [2011]. The mixed stochastic-singular model assumes similar particles are covered with active surface sites characterized by different nucleation barriers, yet each active site follows the stochastic behavior of ice formation. In Niedermeier's model, a particle can have one or many active sites with different contact angles (Figure 26a). Nucleation of freezing on any single site will result in freezing of the entire droplet. Each site has a different contact angle. As illustrated by Figure 26b, the likelihood of freezing on each site is predicted by a probability function based on its specific contact angle. The larger the standard deviation in contact angles, the more variation is seen in freezing temperatures. The distribution of possible contact angles is such that some particles will have at least one site with the best (lowest) contact angle and other particles will not.

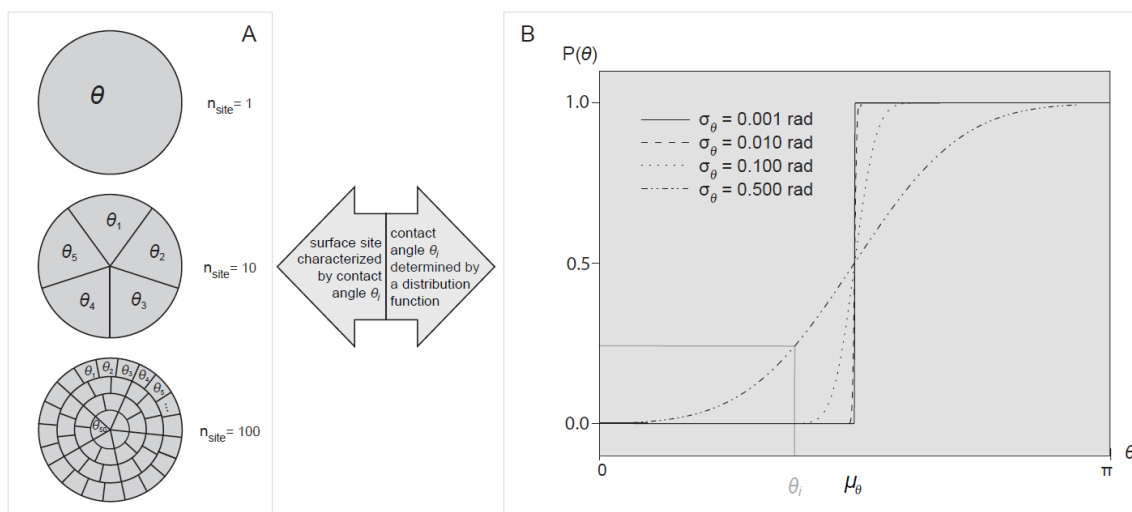


Figure 26. The surface of each particle is divided into a number n_{site} of surface sites, which are characterized by contact angles that have a certain energy barrier. Adapted from: *Niedermeier et al.* [2011].

Figure 27 shows the probability of freezing or fraction frozen as a function of temperature for several hypothetical populations of particles. We note that the shapes of the probability curves in our study are similar to those shown in Figure 27. As seen in Figure 27, for cases in which the standard deviation of contact angles is small, the fraction frozen as a function of temperature follows purely stochastic behavior. The probability curve is basically perpendicular in this case with nearly all freezing events occurring at the same temperature. As the variation in contact angles increases, the probability curve develops a tilt due to a wider spread in freezing temperatures.

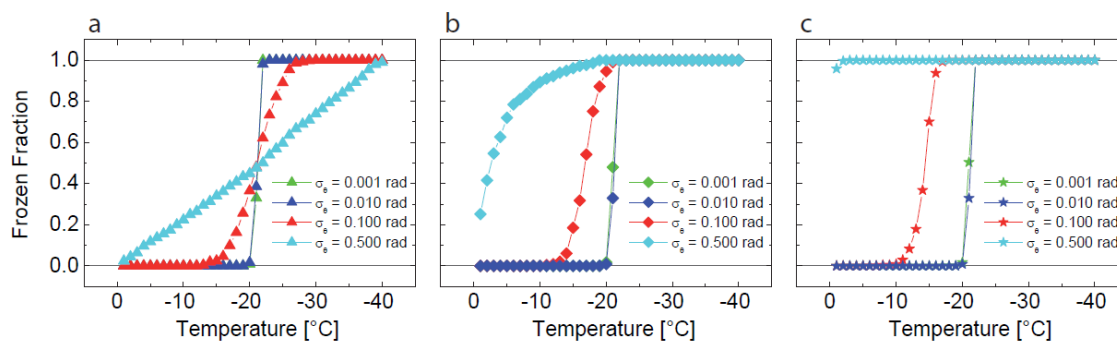


Figure 27. Probability curves similar to those in this study are shown. Figure (a) represents one active site, (b) represents ten active sites, and (c) represents 100 active sites. Different colors indicate different deviations in contact angles. Adapted from: *Niedermeier et al.* [2011].

Next we consider our own results in the context of the mixed stochastic-singular model. Recall that in Figure 23b, the empirical probability curves were more vertical and closer to the theoretical probability curve based on the stochastic theory. Figure 23b is similar to the shape of the dark blue curves in graphs (a), (b) and (c) in Figure 27, which represents a relatively small variation in contact angle where each particle contains 1, 10 or 100 active sites, respectively. The likeness between modeled results and our experimental data suggests that the contact angles on active sites in anthracene samples were all very similar. Next we consider the variation in freezing temperature seen for phenanthrene in Figure 23c. These data more follow the red curve in graphs (a), (b), and (c) in Figure 27 in which a slightly greater variation in contact angle on sites on various particles is assumed. The likeness suggests a greater variability in active sites in phenanthrene than anthracene. This is consistent with the lower and possibly less uniform oxidation of the phenanthrene relative to the other PAHs in this study [*Perraudin et al.*, 2007b]. However, other variability in surface properties within the

sample of oxidized phenanthrene may be causing the variability in freezing temperature. The experimental results are further complicated by particle break-up, which was seen in one experiment. Particle break-up, which exposes more active sites, may be the cause of anomalously warmer freezing temperatures.

The mixed stochastic-singular model may also aid in interpretation of our results for soot, though they are not as straightforward. As seen in Figure 23a, the results for 50 μm oxidized soot are the most variable of all IN in this study. Following the logic of Niedermeier, this indicates a broad range in contact angles (or overall nucleation efficiency) of various active sites. Recall that the oxidized soot of 50 μm diameter activated at very warm temperatures from -8 to -15 $^{\circ}\text{C}$ for the first few cycles, then exhibited freezing temperatures near that of fresh soot, clearly seen in Figure 24. The question remains as to why this occurred for only this size of oxidized soot. One possibility is that some IN may have highly efficient active sites enhanced by sharp edges or cracks that can initiate freezing. It is conceivable that cracks present in the oxidized 50 μm soot due to its small size caused initially warm temperatures. These cracks may have been filled after the first few experimental cycles. Without the sharp edges present to initiate freezing, colder freezing temperatures resulted. Regardless of what caused the variability for all IN experiments, the freezing temperatures for oxidized and fresh IN are significantly different at the 99% confidence level.

4. ATMOSPHERIC IMPLICATIONS AND CONCLUSIONS

This study focused on exploring the ice nucleation ability of two aerosols, soot and PAHs, before and after ozone oxidation. FTIR showed surface oxidation occurred as evidenced by the formation of carboxylic C=O bonds in the FTIR spectra of exposed samples. This led to more wettable particles, as seen by improved propensity of the soot and PAH particles to act as IN. The oxidized samples of soot and PAHs caused a warmer freezing temperature to occur. For some oxidized IN, a change in freezing mechanism also occurred. Oxidized soot became hydrophilic instead of hydrophobic and immersed into the water droplet. Immersion freezing typically occurs at temperatures 4-5 °C cooler for unexposed IN of like compositions [Durant and Shaw, 2005; Shaw *et al.*, 2005]. However, it appears that either the change in temperature due to mechanism did not occur here or if it did, the opposite change due to chemical aging was much greater. The fresh and oxidized anthracene samples froze by the mechanism of contact freezing, in which the PAH particle remained at the surface of the water droplet, yet was inside the droplet. Droplets containing the oxidized anthracene sample froze at warmer temperatures than fresh anthracene despite the lack of change in freezing mechanism. It appears that the warmer freezing temperature is due to the chemical change of the anthracene. Fresh phenanthrene also activated by contact freezing. However, oxidized phenanthrene froze by the contact and immersion method causing variation in temperature. Regardless of the variability, the oxidized phenanthrene froze at a significantly warmer temperature on average than fresh phenanthrene. Like soot, fresh pyrene froze by contact and oxidized pyrene froze by immersion method. Oxidized soot

and pyrene consistently froze by immersion freezing at warmer temperatures, albeit with great variability. Overall, the effects of oxidizing IN overrides variation in freezing mechanism, resulting in warmer freezing temperatures regardless of freezing mechanism. Future work should include careful positioning of oxidized PAH samples on the droplet to force either contact or immersion freezing to further explore the effect of freezing mechanism on temperatures.

On average, fresh soot (three sizes combined) froze at $-23.4\text{ }^{\circ}\text{C}$ with a standard deviation of 1.2. On average, oxidized soot froze at $-20.6\text{ }^{\circ}\text{C}$ with a standard deviation of 2.3. The PAHs in this study exhibited unique behavior in regards to their ice nucleation abilities. Fresh anthracene froze at an average temperature of $-23.7\text{ }^{\circ}\text{C}$ with a standard deviation of 1.1, and oxidized anthracene froze at an average temperature of $-20.9\text{ }^{\circ}\text{C}$ with a standard deviation of 0.8. Fresh phenanthrene froze at an average temperature of $-23.9\text{ }^{\circ}\text{C}$ with a standard deviation of 1.2, and oxidized phenanthrene froze at an average temperature of $-22.4\text{ }^{\circ}\text{C}$ with a standard deviation of 2.43. Fresh pyrene froze at an average temperature of $-21.3\text{ }^{\circ}\text{C}$ with a standard deviation of 1.2, and oxidized pyrene froze at an average temperature of $-19.3\text{ }^{\circ}\text{C}$ with a standard deviation of 2.4. The variability that occurred during experiments may be due to a large variation of contact angles on the surface of the IN depending on the specific particle chosen for each experiment. Taken as a whole, freezing temperatures between soot and PAHs are similar with 50% of the particles frozen by $-23\text{ }^{\circ}\text{C}$ in all fresh cases and at $-21\text{ }^{\circ}\text{C}$ in all oxidized cases. This implies that both aerosols would act in the same similar manner in the

atmosphere. Further, our results suggest that chemical aging improves the ice nucleation ability of aerosols.

This study used classical nucleation theory to calculate heterogeneous nucleation rate, wetting parameter, and probability. Soot and PAH freezing temperatures were used to create empirical probability curves that were helpful in finding the wetting parameter for each IN type. Empirical probability curves also showed that more variability occurred when IN exhibited singular behavior, and less variability occurred in freezing temperatures when the IN exhibited more stochastic behavior. Our results proved that oxidized IN are more efficient than fresh IN due to a smaller wetting parameter, a higher nucleation rate, and a higher probability of freezing. The most efficient PAH was pyrene, while the least efficient was phenanthrene. Overall, the most efficient IN in this study are oxidized pyrene particles. These heterogeneous ice nucleation rates are useful as parameters to input into global climate models to further explore how ice nucleation impacts climate change.

This study showed that the differing sizes of soot particles did not affect freezing temperatures significantly. The change in size also did not have a clear impact on nucleation efficiency. BET surface area measurements show that changing the size of the particle does not change the specific surface area measurement. BET surface area was used when calculating a new wetting parameter, new probability curves, and new heterogeneous nucleation rates for fresh and oxidized soot. The f values found by calculating the 50% probability for each IN (fresh and oxidized) were higher than those found when using geometric surface area. The probability curves were very similar when

using BET, and the nucleation rates were less efficient. It is proposed that the geometric surface area overestimates how efficient soot particles are as IN because the calculations assume soot is spherical and nonporous.

When soot and PAHs are emitted into a polluted environment, they will most likely be exposed to an oxidant like ozone. This means that these aerosols will activate as IN at a warmer temperature in the atmosphere than fresh soot or PAHs. It is believed that oxidized soot freezing by the immersion mechanism would occur at higher altitudes in the atmosphere, while fresh soot would freeze by contact mechanism near the surface, where more uncoated particles are located. The same idea would apply to PAH particles in the atmosphere; however, this is more uncertain as more research is needed to make definite conclusions for PAH as IN. Heterogeneous ice nucleation is an important mechanism in the atmosphere at warmer temperatures. Ice clouds have the ability to reflect incoming radiation, which leads to negative radiative forcing. This indirect effect on climate change can help reduce the amount of radiation reaching the surface of the Earth and help to offset global warming due to increased carbon dioxide emissions.

REFERENCES

- Aubin, D. G., and J. P. Abbatt (2003), Adsorption of gas-phase nitric acid to n-hexane soot: Thermodynamics and mechanism, *Journal of Physical Chemistry A*, 107(50), 11030-11037.
- Bedjanian, Y., and M. L. Nguyen (2010), Kinetics of the reactions of soot surface-bound polycyclic aromatic hydrocarbons with O₃, *Chemosphere*, 79(4), 387-393.
- Bedjanian, Y., M.L Nguyen, and G. Le Bras (2010), Kinetics of the reactions of soot surface-bound polycyclic aromatic hydrocarbons with the OH radicals, *Atmospheric Environment*, 44(14), 1754-1760.
- Brunauer, S., P.H. Emmett, and E. Teller (1938), Adsorption of gases in multimolecular layers, *J. Am. Chem. Soc.*, 60, 309-319.
- Calvert, J. G. (2002), *The mechanisms of atmospheric oxidation of aromatic hydrocarbons*, 556 pp., Oxford University Press, New York.
- Chughtai, A. R., J. A. Jassim, J. H. Peterson, D. H. Stedman, and D. M. Smith, (1991), Spectroscopic and solubility characteristics of oxidized soots, *Aerosol Science and Technology*, 15(2), 112-126.
- Cooper, W. A. (1974), Possible mechanism for contact nucleation, *J. Atmos. Sci.*, 31(7), 1832-1837.
- Decesari, S., M. C. Facchini, E. Matta, M. Mircea, S. Fuzzi, et al. (2002), Water soluble organic compounds formed by oxidation of soot, *Atmospheric Environment*, 36(11), 1827-1832.
- Demott, P. J. (1990), An Exploratory-Study of Ice Nucleation by Soot Aerosols, *J. Appl. Meteorol.*, 29(10), 1072-1079.
- Demott, P. J. (1995), Quantitative descriptions of ice formation mechanisms of silver iodide-type aerosols, *Atmospheric Research*, 38(1-4), 63-99.
- Diehl, K., and S. K. Mitra (1998), A laboratory study of the effects of a kerosene-burner exhaust on ice nucleation and the evaporation rate of ice crystals, *Atmospheric Environment*, 32(18), 3145-3151.
- Durant, A. J., and R. A. Shaw (2005), Evaporation freezing by contact nucleation inside-out, *Geophys. Res. Lett.*, 1-32, L20184.

- Dymarska, M., Benjamin J. Murray, Limin Sun, Michael L. Eastwood, and Daniel A. Knopf, et al. (2006), Deposition ice nucleation on soot at temperatures relevant for the lower troposphere, *J. Geophys. Res.*, *111*, 1-9, D04204.
- Finlayson-Pitts, B. J., and J. N. Pitts (1986), *Atmospheric Chemistry: Fundamentals and Experimental Techniques*, xxviii, 1098 pp., Wiley, New York.
- Finlayson-Pitts, B. J., and J. N. Pitts (2000), *Chemistry of the Upper and Lower Atmosphere: Theory, Experiments and Applications*, xxii, 969 pp., Academic Press, London.
- Fletcher, N. H. (1962), *The Physics of Rainclouds*, 386 pp., Cambridge University Press, Cambridge, U.K.
- Fletcher, N. H. (1969), Active sites and ice crystal nucleation, *J. Atmos. Sci.*, *26*(6), 1266-1271.
- Fornea, A. P., S. D. Brooks, J. B. Dooley, and A. Saha (2009), Heterogeneous freezing of ice on atmospheric aerosols containing ash, soot, and soil, *Journal of Geophysical Research-Atmospheres*, *114*, 1-12, D13201.
- Fukuta, N. (1975), Study of mechanism of contact ice nucleation, *J. Atmos. Sci.*, *32*(8), 1597-1603.
- Gorbunov, B., et al. (2001), Ice nucleation on soot particles, *J. Aerosol. Sci.*, *32*(2), 199-215.
- Gregg, S. J., et al. (1967), Adsorption Surface Area and Porosity, *Journal of the Electrochemical Society*, *114*(11), 279C.
- Hoose, C., J. E. Kristjansson, J. P. Chen, and A. Hazra (2010), A Classical-Theory-Based Parameterization of Heterogeneous Ice Nucleation by Mineral Dust, Soot, and Biological Particles in a Global Climate Model, *J. Atmos. Sci.*, *67*(8), 2483-2503.
- Hung, H. M., Y. Katrib, and S. T. Martin (2005), Products and mechanisms of the reaction of oleic acid with ozone and nitrate radical, *Journal of Physical Chemistry A*, *109*(20), 4517-4530.
- Hunter, R. J. (1993), *Introduction to Modern Colloid Science*, Oxford Science Publications, New York.
- IPCC (2007), *Climate Change 2007: The Physical Science Basis*. Summary for Policy makers. Contribution of Working group 1 to the fourth assessment report of the Intergovernmental Panel for Climate Change, 21 pp., IPCC Secretariat, Geneva.

- James, D. W. (1968), The Thermal Diffusivity of Ice and Water between -40 and $+60^{\circ}$ C, *Journal of Materials Science*, 3(5), 540-543.
- Kahan, T. F., N. O. A. Kwamena, and D. J. Donaldson (2006), Heterogeneous ozonation of polycyclic aromatic hydrocarbons on organic films, *Atmospheric Environment*, 40, 3448-3459
- Kanji, Z. A., and J. P. D. Abbatt (2006), Laboratory studies of ice formation via deposition mode nucleation onto mineral dust and n-hexane soot samples, *Journal of Geophysical Research-Atmospheres*, 111(D16), 1-10.
- Kanji, Z. A., O. Florea, and J. P. D. Abbatt (2008), Ice formation via deposition nucleation on mineral dust and organics: dependence of onset relative humidity on total particulate surface area, *Environmental Research Letters*, 3(2), 1-7.
- Kotzick, R., U. Panne, and R. Niessner (1997), Changes in condensation properties of ultrafine carbon particles subjected to oxidation by ozone, *J. Aerosol. Sci.*, 28(5), 725-735.
- Kotzick, R., and R. Niessner (1999), The effects of aging processes on critical supersaturation ratios of ultrafine carbon aerosols, *Atmospheric Environment*, 33(17), 2669-2677.
- Kwamena, N. O. A., M. E. Earp, C. J. Young, and J. P. D. Abbatt (2006), Kinetic and product yield study of the heterogeneous gas-surface reaction of anthracene and ozone, *Journal of Physical Chemistry A*, 110(10), 3638-3646.
- Langham, E. J., and B. J. Mason (1958), The heterogeneous and homogenous nucleation of supercooled water, *Proceedings of the royal society of london series a-mathematical and physical sciences*, 247(1251), 493 pp.
- Lary, D. J., D. E. Shallcross, and R. Toumi (1999), Carbonaceous aerosols and their potential role in atmospheric chemistry, *Journal of Geophysical Research-Atmospheres*, 104(D13), 15929-15940.
- Levitt, N. P., R. Y. Zhang, Xue, H. X., and Chen, J. M. (2007), Heterogeneous chemistry of organic acids on soot surfaces, *Journal of Physical Chemistry A*, 111(22), 4804-4814.
- Mason, L. (2009), Linking Chemical Changes in Soot and Polyaromatics to Cloud Droplet Formation, Thesis, Texas A&M University, College Station.
- Niedermeier, D., R. A. Shaw, S. Hartman, H. Wex, and T. Claus (2011), Heterogeneous ice nucleation: Bridging stochastic and singular freezing behavior, *Atmospheric Chemistry and Physics Discussion*, 11(1), 3162-3180.

- Penner, J. E., H. Eddleman, and T. Novakov (1993), Towards the Development of a Global Inventory for Black Carbon Emissions, *Atmospheric Environment Part a- General Topics*, 27(8), 1277-1295.
- Perraudin, E., H. Budzinski, and E. Villenave (2007a), Identification and quantification of ozonation products of anthracene and phenanthrene adsorbed on silica particles, *Atmospheric Environment*, 41(28), 6005-6017.
- Perraudin, E., H. Budzinski, and E. Villenave (2007b), Kinetic study of the reactions of ozone with polycyclic aromatic hydrocarbons adsorbed on atmospheric model particles, *Journal of Atmospheric Chemistry*, 56(1), 57-82.
- Popovicheva, O., E. Kireeva, N. Persiantseva, T. Khokhlova, N. Shonija, et al. (2008a), Effect of soot on immersion freezing of water and possible atmospheric implications, *Atmospheric Research*, 90(2-4), 326-337.
- Popovicheva, O. B., N. M. Persiantseva, V. Tishkova, N. K. Shonija, and N. A. Zubareva (2008b), Quantification of water uptake by soot particles, *Environmental Research Letters*, 3(2), 1-12.
- Pruppacher, H. R., and J. D. Klett (Eds.) (1997), *The Microphysics of Clouds and Precipitation*, 2nd ed., 954 pp., Kluwer Academic Publishers, Dordrecht, The Netherlands.
- Rosenberg, A. J. (1956), Rapid, Precise Measurements of Krypton Adsorption and the Surface Area of Coarse Particles, *J. Am. Chem. Soc.*, 78(13), 2929-2934.
- Rosenfeld, D. (2000), Suppression of Rain and Snow by Urban and Industrial Air Pollution, *Science*, 287(5459), 1793-1796.
- Seinfeld, J. H., and S. N. Pandis (2006), *Atmospheric chemistry and physics : from air pollution to climate change*, 2nd ed., xxviii, 1203 pp., John Wiley, Hoboken, N.J.
- Shaw, R. A., A.J. Durant, and Y. Mi (2005), Heterogeneous surface crystallization observed in undercooled water, *J. Phys. Chem. B*, 109(20), 9865-9868.
- Vali, G. (1985), Nucleation terminology, *J. Aerosol. Sci.*, 16(6), 575-576.
- Vali, G. (2008), Repeatability and randomness in heterogeneous freezing nucleation, *Atmos. Chem. Phys.*, 8(16), 5017-5031.
- Weingartner, E., H. Burtscher, and U. Baltensperger (1997), Hygroscopic properties of carbon and diesel soot particles, *Atmospheric Environment*, 31(15), 2311-2327.

Yanazawa, H., K. Ohshika, and T. Matsuzawa (2000), Precision evaluation in Kr adsorption for small BET surface area measurements of less than 1 m², *Adsorpt.-J. Int. Adsorpt. Soc.*, 6(1), 73-77.

Yau, M. K. and R.R. Rogers (1989), *A Short Course in Cloud Physics*, 3rd ed., Pergamon Press, New York.

VITA

Name: Katie Ann Suter

Address: Texas A&M Department of Atmospheric Sciences
c/o Dr. Sarah Brooks
1204 Eller O&M, 3150 TAMU
College Station, TX 77843-3150

Email Address: k.suter387@gmail.com

Education: B.S., Meteorology, Texas A&M University, 2009
M.S., Atmospheric Sciences, Texas A&M University, 2011